Viscous Energy Dissipation and Strain Partitioning in Partially Molten Rocks

BENJAMIN K. HOLTZMAN[1]*, DAVID L. KOHLSTEDT[1] AND JASON PHIPPS MORGAN[2]

[1]DEPARTMENT OF GEOLOGY AND GEOPHYSICS, UNIVERSITY OF MINNESOTA, 310 PILLSBURY DRIVE SE, MINNEAPOLIS, MN 55455, USA

[2]DEPARTMENT OF EARTH AND ATMOSPHERIC SCIENCES, CORNELL UNIVERSITY, ITHACA, NY 14853-1504, USA

We develop a steady-state fluid-mechanical analysis describing the effect of strain partitioning on viscous energy dissipation. As observed in experimental studies of shear deformation of partially molten rocks, strain partitions when melt segregates because viscosity is reduced in regions of elevated melt fraction. The equations derived here are based on parameters measured in experiments, describing the evolution of melt distribution and rheological properties. We find that the dissipation depends strongly on the configuration of the melt-rich network of shear zones, including the average angle, volume fraction of melt and amplification of strain rate in the melt-rich bands. Minima in energy dissipation as a function of band angle develop, corresponding to configurations of melt networks that minimize the difference in mean stress between the band and the non-band regions. We propose that the organization of band networks occurs by the interplay between strain localization and viscosity variations associated with melt segregation. The band networks maintain a steady-state angle during shear by continuously pumping melt through the network. The development of strain partitioning in melt-rich networks will modify the energetics of melting and melt transport by efficiently extracting melt and reducing effective viscosity.

KEY WORDS: *melt transport; rheology; self-organization; strain localization; strain partitioning*

INTRODUCTION

Most regions in the mantle where large volumes of melt are produced are also deforming intensely, such as mid-ocean ridges, subduction zones and sites of plume–lithosphere interactions. We have demonstrated in laboratory deformation experiments on partially molten rocks that the deviatoric stress causing deformation of the rock can also drive small fractions of melt to segregate and organize into melt-rich networks (Holtzman *et al.*, 2003a). We subsequently showed that melt transport and deformation are very closely coupled processes (Holtzman *et al.*, 2003b). Similar coupled processes of weakening and strain localization occur in many systems, from metals to solid state rocks to granular materials, due to many causes of local weakening like grain size reduction or solid phase separation. One objective of this study is to quantify macroscopic effects of meso-scale strain partitioning on the effective viscosity, with the aim of developing a simple means of scaling the consequences of strain partitioning to rheological conditions relevant to the Earth. However, the primary goal is to derive an analysis of the steady-state process that helps us to understand the dynamics of the observed self-organization of melt and solid during strain partitioning.

For applications to processes in the Earth, melt segregation and strain partitioning will strongly influence seismic, fluid transport and rheological properties. In this paper, we will discuss the latter two. Numerous lines of evidence suggest that much of the transport of melt occurs in chemically isolated channels (Kelemen *et al.*, 1997). Thus, large-scale melt transport must be preceded by segregation into channels. When melt segregates, viscosity becomes heterogeneous because it is highly melt fraction-dependent. Strain then partitions between weak and strong regions, modifying the stress field. The weak regions interact and self-organize into a connected network. Strain localization occurs at much smaller scales than are describable in current continuum geodynamic models of any of the regions in the Earth where they

*Corresponding author. Present address: Lamont Doherty Earth Observatory, Columbia University, Palisades, NY, USA. Fax: 845 365 8150. E-mail: benh@ldeo.columbia.edu

will be important. However, the effects of segregation on melt transport and on the effective viscosity of regions of the mantle and crust will likely be influential at the larger scales of these regional models (Buck and Su, 1989).

That melt segregation and channel formation can be driven by deviatoric stress was predicted near the end of the 20th century (Stevenson, 1989). An attempt at modeling the initiation of melt segregation and growth of melt-rich bands in simple shear has been performed by Spiegelman (2003), expanding the analysis of Stevenson (1989). Our study represents a very different approach. We do not attempt to solve for the growth rate of melt-rich perturbations; instead, we characterize the viscous energy dissipation in steady state as a function of the configuration of (melt-rich) weak zones. The analysis is written in terms of parameters that are measured directly from melt distributions in experimental samples, and thus should be amenable to comparison with experimental results.

Viscous energy dissipation, the energy produced by deformation of a fluid (or simply dissipation) is a quantity that connects fluid dynamics with thermodynamics (Mase, 1973). The concept appears in a range of contexts, including the energetics of plate tectonics and mantle convection (Froideveaux, 1973; Yuen and Schubert, 1977; Bercovici and Ricard, 2003), of mantle melting and melt/rock interactions (Asimow, 2002), and of self-organizing non-equilibrium systems (Nicolis and Prigogine, 1977; de Groot and Mazur, 1984). Dissipation is calculated to explore thermal weakening instabilities in deforming, temperature-sensitive materials with and without stress-dependent rheological properties (Yuen and Schubert, 1977; Kameyama et al., 1997). Here, we explore the effect of melt segregation and strain partitioning on dissipation in partially molten systems, with implications for a wide range of petrologic/geodynamic problems (Table 1).

Summary of experimental studies

The observed melt distribution reflects the state of stress in the sample at the time of quenching, as shown in Fig. 1 and 2a. This statement is especially easy to justify for samples in which dissipation and effective viscosity reach a steady state, indicated by constant values of stress and strain rate for much of the duration of the deformation, as shown in Fig. 2b. Our aim is to relate the properties of this melt distribution with the measured rheological properties. A successful theory should explain the following observations:

(1) The initial compaction length (of the system with unsegregated melt), δ_c, is an important characteristic length scale in the behavior of these systems, because it predicts the conditions under which melt segregation occurs and the spacing between largest bands, δ_{sp}, is

Table 1: List of symbols

Symbol	Meaning
T	Temperature
$\mathcal{S}$	Entropy
$\Phi_{t,b,n}$	Dissipation (total, bands, non-bands)
$\Phi_\circ$	Dissipation for a homogeneous system with $\phi = \phi_t$
γ	Shear strain
γ_f	Final shear strain
$\dot{\gamma}$	Shear strain rate
Φ_f	Final value of dissipation, associated with γ_f
η	Viscosity
n	Stress exponent ($\dot{\gamma} \propto \tau^n$)
$\eta_\circ$	Melt-free viscosity
λ	Weakening factor
σ	Differential stress ($\sigma_{11} - \sigma_{33}$)
τ	Shear stress (σ_{13})
$\Delta\tau^{b-n}$	Shear stress difference between band and non-band
$\phi_{t,b,n}$	Melt fraction, total, band, non-bands
$\phi_{b,n}$	Melt fraction normalized by ϕ_t
$a_{b,n}$	Area fraction of bands and non-bands (e.g. a_{bands}/a_{total})
S_t	Total segregation $= \phi_b a_b$
c	Exponent in S_t definition
α	Band angle relative to total shear plane
β	Non-band angle
$\rho_{t,b,n}$	Density of the melt-solid composite
$\mathbf{v}_t$	Average velocity of the whole sample (total)
$\mathbf{v}_b$	Average velocity of the bands
$\mathbf{v}_n$	Average velocity of the non-bands
T, B, N	Velocity gradient tensors ($\partial v_i/\partial x_j$)
b_{13}	Components of B ($\partial v_1/\partial x_3$)$_b$, etc.
B^R	Rotated velocity gradient tensors
$\dot{\varepsilon}_{t,b,n}$	Strain rate tensors (e.g. decomposed B^R)
$\dot{\gamma}^{II}$	Second invariant of the stress tensor
p_b	Strain partitioning factor

proportional to δ_c in a range of melt-rock systems (Holtzman et al., 2003a). While the band spacing enters only implicitly, but not explicitly in this analysis (i.e. dissipation does not vary with band spacing), this observation is an essential part of the larger problem.

(2) When melt segregates, strain partitions between melt-rich networks and melt-poor lenses, strongly modifying the patterns of flow and orientations of the stress tensors in the sample, as revealed by measurements of lattice preferred orientations (LPO) (Holtzman et al., 2003b).

(3) Melt bands exist with a bimodal distribution of angles (0–30°) shown in Figs 1 and 2a. This pattern is common. In general, large bands are found at higher
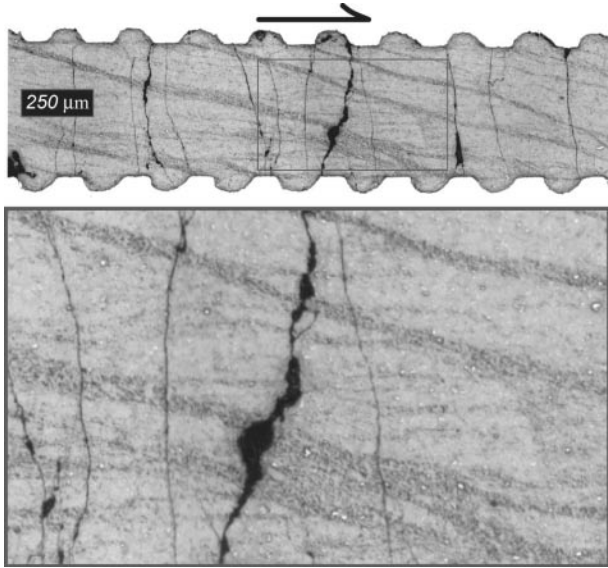
Fig. 1. An example of one experiment (PI-1096), olivine + chromite (4:1) + 4 vol% MORB, constant strain rate, $\gamma = 3.4$. Melt-rich bands are the darker gray regions from 0° to 25° to the shear plane (sample wall). Black subvertical cracks form during the quench and do not affect the melt distribution. The serrated boundaries reflect grooves in the piston walls cut to grip the sample during shear.
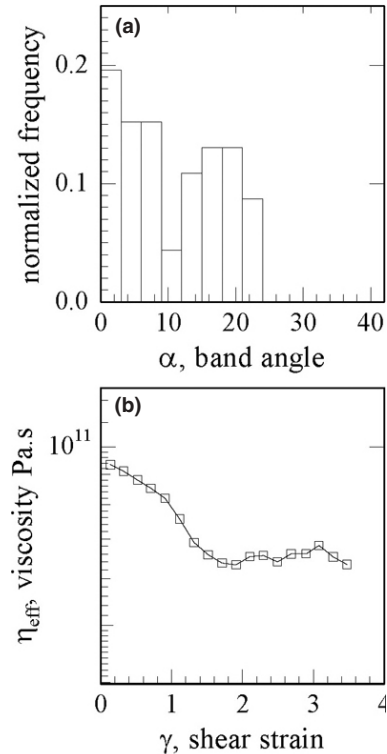

Fig. 2. An example of one experiment (PI-1096). (a) Distribution of band angles. In this sample, the distribution appears to be bimodal, consistent with the image in Fig. 1. (b) Effective viscosity as a function of shear strain. Note that in an experiment performed under constant displacement rate conditions such as this one, the dissipation values will follow a similar trajectory.

angles and narrow bands at lower angles. The thicker, higher angle population is rotated an average of $\approx 20°$ from the shear plane regardless of finite shear strain (Holtzman *et al.*, 2003a). We propose that this bimodal distribution is the signature of a connected network.

(4) The changes in effective viscosity in a sample, shown in Fig. 2b, begin with a gradual decrease and then reach a steady state at a shear strain of $\gamma = 1$. We hypothesize that the weakening is associated with the formation of a connected network of melt bands; steady state occurs when the kinetics of melt migration and reorganization are balanced by the kinetics of solid deformation during melt segregation.

The main purpose of this study is to understand what properties of the deforming system control the observed dissipation and enable the angular stability of a network to exist. To do so, we calculate the total viscous energy dissipation as the sum of the contributions from the band and non-band regions, in terms of parameters whose values are measured in our experimentally deformed samples, a_b, ϕ_b and α. These equations offer an explanation for the observed preference of $\alpha \approx 20°$. Even though the solutions below involve many simplifying assumptions, they provide useful insights and suggest directions for further study.

Viscous energy dissipation

The viscous energy dissipation is the contribution to the total energy made by irreversible deformational work per

unit time and volume, that is, the power per unit volume. We base our analysis on the dissipation because the energies of separate parts of a system are additive, whereas the viscosities are generally not (except in specific cases). We relate changes in melt distribution to changes in the energy of the system as a way of quantifying the effects on the rheological behavior of the system with time. An expression for the first law of thermodynamics (Batchelor, 1967, p. 153, modified from equations 3.4.4 and 3.4.5, respectively, pulling ρ out of the definition of dissipation), describing the total change in internal energy, E, with respect to time, t, in a fluid is

$$\frac{DE}{Dt} = \frac{1}{\rho}\left[-P_s\dot{\varepsilon}_{ii} + \Phi + \frac{\partial}{\partial x_i}\left(\kappa\frac{\partial T}{\partial x_i}\right)\right]. \quad (1)$$

The second term on the right-hand side (RHS) is the dissipation function,

$$\Phi = \eta_{\text{eff}}\left(\dot{\varepsilon}_{ij}\dot{\varepsilon}_{ij} - \frac{1}{3}\dot{\varepsilon}_{ii}^2\right) \quad (2)$$

and P_s is pressure in the solid, κ is thermal conductivity, T is temperature, η_{eff} is effective shear viscosity, and $\dot{\varepsilon}_{ij}$ is

the ith, jth component of the strain rate tensor. [Note that Batchelor includes the density in the dissipation function while other sources do not (Mase, 1975; Ranalli, 1987)]. The first term on the RHS of equation (1) describes the contribution of the volumetric part of the deformation (i.e. due to changes in pressure). At the high T and P conditions of our experiments, 'dilatancy' is only local, accommodated by decompaction in one region and compaction in another during melt segregation, both of which are forms of work, so they contribute to the measured dissipation. (In Batchelor's definition of energy dissipation, this volumetric work is removed. However, in the measured data, we cannot remove the effects of this irreversible loss of energy. In the following analysis, we focus on shear-dominated deformation and assume that the volumetric part is negligible). The third term on the RHS is the rate of heat gain/loss, which is negligible during experiments at constant temperature, so $\partial T / \partial x_i = 0$. A closely related equation describes the entropy production

$$T \frac{DS}{Dt} = \frac{DE}{Dt} \qquad (3)$$

where S is the entropy. In our experiments, the main contribution to the entropy production comes from Φ.

Measuring the dissipation and effective viscosity as a function of strain in experiments provides insight into the changing rheological behavior of the sample as the melt distribution evolves. Taking the simple expression for the shear stress, $\tau = \eta_{\mathrm{eff}} \dot{\gamma}$, where $\dot{\gamma}$ is the shear strain rate, the dissipation can be written as

$$\Phi = \tau \dot{\gamma} = \eta_{\mathrm{eff}} \dot{\gamma}^2. \qquad (4)$$

To calculate Φ and η_{eff} from experimental data, we use the expressions

$$\Phi_i = \tau_i \dot{\gamma}_i \quad \text{and} \quad \eta_i^{\mathrm{eff}} = \frac{\tau_i}{\dot{\gamma}_i} \qquad (5)$$

where the subscript i indicates that the value is measured and recorded during the experiment at small strain increments. Each point in Fig. 2b represents the quotient of stress and strain rate at a given finite strain. In discussion, we will compare the results of the analysis with the measured values of Φ and η_{eff}.

STEADY STATE VISCOUS ENERGY DISSIPATION: GENERAL DERIVATION

Here, we present the most general equations in this analysis, describing the mass balance and rheological properties. The approach to solving for the strain rates is developed in the next section. To characterize the segregation of melt and the partitioning of strain rate
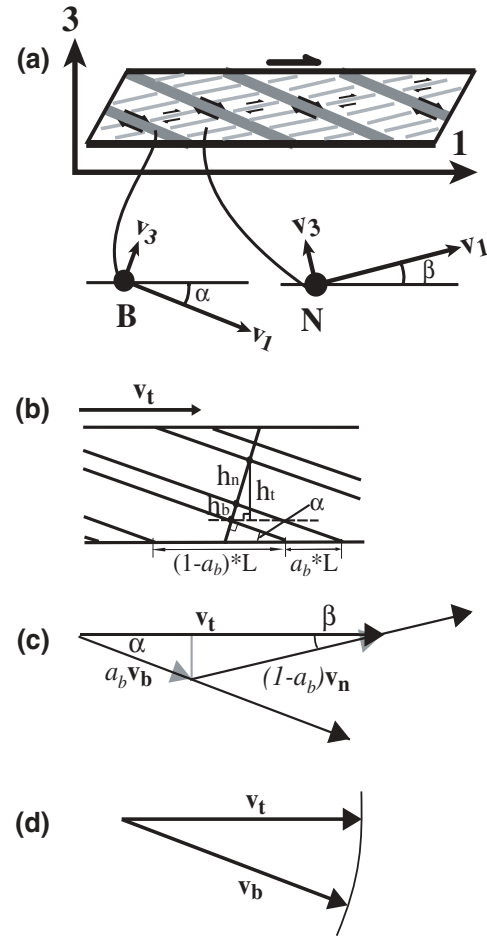

Fig. 3. The model setup. (a) The reference frames for the dissipation calculations. The thick gray lines represent the bands and the thin gray lines represent the shear plane in the non-bands. The lower diagrams illustrate the reference frames for the velocity gradient tensors, **B** and **N**, for the bands and non-bands. (b) The 'unit cell' whose fundamental length scale is the distance between two bands, or the thickness of the lenses. These length scales are normalized and treated as area fractions a_{b} and $1 - a_{\mathrm{b}}$. (c) The vector diagram illustrating that the average velocities weighted by area fraction (in 2D) must sum to the total average velocity. This diagram is the basis for most of the analysis and derivation of strain rates. (d) The limit to real solution. $\mathbf{v}_{\mathrm{b}}$ cannot be larger than $\mathbf{v}_{\mathrm{t}}$ or else the solution makes no physical sense. The related mathematical limitation is derived in the text.

between the melt-rich bands and the melt-depleted lenses, we make two main simplifications:

(1) The system is in a steady state (or a 'stationary state', de Groot and Mazur, 1984) such that the *average* heterogeneous spatial distributions of melt and strain rate are constant in time, though, the local distribution of melt is constantly changing. We do not assume that Φ is minimized; rather, we demonstrate that geometric conditions exist for which it is minimized.

(2) The bands and the lenses are 'boundary layers' characterized by laminar flow (Batchelor, 1967, section 5.7), as illustrated in Fig. 3. In this approximation,

we assume that each laminar flow field can be characterized by a vector representing the average velocity. These two vectors have compatibility conditions, but there is no spatially discretized compatibility between the margins of these velocity fields. From this simplification the strain rates are derived below.

As implied by equation (1), contributions to the total energy are additive, $\Phi_t = \sum_{i=1}^{n} \Phi_i$. Equation (2) can be simplified by assuming that the dilatancy term is much smaller than the shear term:

$$\Phi = \eta_\phi \dot{\varepsilon}_{ij} \dot{\varepsilon}_{ij}. \tag{6}$$

Thus, the dissipation in a strain-partitioned system is described by

$$\Phi_t = a_b \Phi_b + (1 - a_b) \Phi_n \tag{7}$$

where the subscripts b, n and t refer to the melt-rich bands, melt-depleted non-band regions and the total system, respectively, and a_b is the area (or volume) fraction of bands by which the dissipation contributions of the band and non-band regions are weighted. The energy dissipation in the bands and lenses is calculated below with expressions that relate gradients in the band and non-band velocity fields. First, we describe how we parameterize the melt distribution and the melt fraction-dependent viscosity.

Melt configuration and mass conservation

In this analysis, as with the experiments, melt fraction is constant and the whole system is closed. The equations are written in terms of average properties of the melt distribution. Melt 'configuration' refers to the ensemble of measurable qualities describing the melt distribution in a rock, experimental or natural. Melt-rich bands and melt-depleted lenses are defined as regions with higher and lower values of ϕ than the average in the sample, ϕ_t, respectively. The area fraction, a_b, and average melt fraction in the bands, ϕ_b, serve as rough measures of the effectiveness of melt segregation and allow us to calculate average rheological properties of the two types of regions. The non-dimensional area fraction of bands and non-bands are simply

$$a_b = \frac{a_b^o}{a_t^o} \quad \text{and} \quad a_n = \frac{a_n^o}{a_t^o} \tag{8}$$

and the mass balance for segregated melt can be described as

$$a_t^o \phi_t = a_b^o \phi_b + a_n^o \phi_n \tag{9}$$

where ϕ_n is the melt fraction in the melt-depleted, lens or 'non-band' regions, and the o indicates the dimensional area. Normalizing by a_t^o, we obtain

$$\phi_t = a_b \phi_b + (1 - a_b) \phi_n \tag{10}$$

and by ϕ_t,

$$\phi_b' a_b + (1 - a_b) \phi_n' = 1 \tag{11}$$

which is the statement of volume balance (or mass balance for incompressible fluids). From here on, we will refer to ϕ_b as the segregation factor, a measure of the degree of melt segregation, as

$$\phi_b' = \frac{\phi_b}{\phi_t}. \tag{12}$$

And so

$$\phi_n' = \frac{\phi_n}{\phi_t} = \frac{1 - \phi_b a_b}{1 - a_b}. \tag{13}$$

From equation (11), $\phi_b = (1/a_b)[1 - (1 - a_b)\phi_n]$, which says that as the melt fraction in the lenses approaches zero, $\phi_n \to 0$, $\phi_{max} \to 1/a_{max}$. From here on, we drop the primes from the notation.

Here, we define another dimensionless parameter that describes the degree to which melt is segregated. The total segregation factor, $S_t = \phi_b a_b$, ranges from 0 to 1. At $S_t = 1$, no melt remains in the lenses. We can measure this value in experimentally deformed samples. S_t does not uniquely describe the evolution of the melt configuration, but we can define paths that describe various evolutions in terms of S_t. From experimental observations, we know that a_b and ϕ_b increase with increasing strain. A simple equation that fits observed paths of ϕ_b is

$$\phi_b = 1 + (\phi_{max} - 1)(S_t)^c \tag{14}$$

and by definition, $S_t = a_b \phi_b$, so

$$a_b = \frac{S_t}{\phi_b} = \frac{S_t}{1 + (\phi_{max} - 1)(S_t)^c}. \tag{15}$$

The constants can be determined from experimental data. In the following section, we show how this mass balance feeds into the rheological properties.

Melt fraction-dependent viscosity

The strain rate of a melt-free rock may be described by a flow law of the form

$$\dot{\gamma}_{\phi=0} = A \tau^n d^{-m} \exp\left[\frac{-(E^* + PV^*)}{RT}\right] \tag{16}$$

where A is the preexponential term, τ is the shear stress, d is the grain size, E^* is the activation energy for creep, P is the pressure, V^* is the activation volume and R is the gas constant. The effective viscosity ($\eta = \tau/\dot{\gamma}$) can be expressed as (assuming grain size is independent of stress),

$$\eta_{\phi=0} = A^{-1} \tau^{-(n-1)} d^m \exp\left(\frac{E^* + PV^*}{RT}\right). \tag{17}$$

In this analysis, we assume a simple Newtonian ($n = 1$) viscosity even though non-linear dependence of viscosity on stress certainly influences the measured dissipation. (In our experiments, melt segregation and strain partitioning occur for a range of effective stress exponents, from ~ 1 to >3.)

In this paper, we are most interested in the non-linear weakening effect of melt on the viscosity, often parameterized with the expression

$$\eta(\phi) = \eta_{\phi=0} \exp(-\lambda \phi) \qquad (18)$$

an equation based on an empirical fit to experimental creep data (Kelemen *et al.*, 1997). The value of the factor λ is ~ 25 in the olivine + MORB system (Mei *et al.*, 2002; Zimmerman and Kohlstedt, 2004, referred to therein as α). The value for the olivine + chromite + MORB samples is undetermined, but we assume that it is similar. The melt-dependent viscosity can be parameterized in terms of ϕ_b as

$$\eta_b = \eta_{\phi=0} \exp(-\lambda \phi_b \phi_t) \qquad (19)$$

and with a similar expression for η_n, using equation (13). In this study, we only address the changes in dissipation due to the changing melt fraction, leaving to a future study the effects of non-linear dependence of viscosity on stress. This relationship implies that $\dot{\gamma}_\phi / \dot{\gamma}_{\phi=0} = \exp(\lambda \phi)$. Although we leave the degree of strain partitioning as a variable in the system, this relation does enter the derivation below. We emphasize that the part of the analysis dealing with the rheological properties and constitutive relations governing weak zones can be modified for any system, to account for other causes of viscosity variations, for example, by grain size reduction or thermal weakening.

Energy conservation

Ignoring the other contributions to the total energy from equation (1), the statement of partitioned dissipation becomes the energy conservation statement. The definitions of the parameters in this problem are such that most can be directly measured from the experiments: a_b, ϕ_b, ϕ_t, λ, α and $\dot{\gamma}_t$. The unknowns are the strain rates in the band and the non-band regions, but strong constraints may be placed on these values in the following section. In sum, equation (7) becomes

$$\left\{
\begin{array}{ll}
\Phi_t = a_b \eta_b (\dot{\varepsilon}_{ij}^b \dot{\varepsilon}_{ij}^b) + (1 - a_b) \eta_n (\dot{\varepsilon}_{ij}^n \dot{\varepsilon}_{ij}^n) & (a) \\
\eta_b = \eta_0 \exp(-\lambda \phi_b \phi_t) & (b) \\
\eta_n = \eta_0 \exp(-\lambda \phi_n \phi_t) & (c) \\
\phi_n = \dfrac{1 - \phi_b a_b}{1 - a_b} & (d) \\
{}^*\phi_b = 1 + (\phi_{max} - 1)(S_t)^c & (e) \\
{}^*a_b = \dfrac{S_t}{1 + (\phi_{max} - 1)(S_t)^c} & (f)
\end{array}
\right\} \qquad (20)$$

where $\dot{\varepsilon}_{ij}^{b,n}$ are the strain rate tensors for the bands and non-bands rotated into the reference frame of the sample. The '*' indicates that these equations are not essential to the solution and are only used when solved in terms of S_t.

SOLVING FOR STRAIN RATES

The essential remaining piece of this problem is to calculate the strain rate tensors for the band and non-band regions. The general approach is to define the average velocities (using the boundary layer approximation), derive velocity gradient tensors and then decompose those velocity gradient tensors into strain rate tensors. This procedure is outlined in detail in Appendix A, and the results surface at the end of this section. The velocity gradient tensors for the bands and non-bands are defined in their own reference frames. To add them, the tensors are rotated into the sample reference frame, as shown in Fig. 3. While only the total strain rate component is known, the other components can be either neglected or solved for, using simplifications stated below.

To solve for the components of the strain rate tensors analytically, we derive relationships between the components of these tensors that allow the total number of unknowns to be reduced to three:

1. We use a boundary layer approximation to define the average velocity vectors and the relationships between average velocity fields.
2. We impose simple boundary conditions on the above relations and derive a relationship between the shear strain rate in the bands and that in the non-bands.
3. We define a parameter that describes the degree of strain rate partitioning occurring in the system. This dimensionless parameter, p_b, allows us to further reduce the number of unknowns in the system.
4. Finally, we derive a relationship between the band angle α and the non-band angle β.

Boundary layer approximation

The boundary layer approximation, illustrated in Fig. 3, holds that if the velocity gradients normal to the boundary are much greater than the gradients parallel to the wall (and the shear direction), the flow can be described as laminar and a simple average velocity vector can be assigned (Batchelor, 1967, section 5.7). These average velocity vectors for each region sum to the total average velocity vector, $\mathbf{v}_t$, which is the basis for the vector diagram shown in Fig. 3. This rule specifies the interactions between the two velocity fields; there is no other coupling between these fields. In this boundary layer approximation, the stress and velocity compatibility conditions at the interface are not satisfied point-wise. Instead, we derive compatibility conditions for the average velocity fields, which is constrained by the divergence and curl of the average velocity fields. Mass conservation based on the

boundary layer approximation, using the average velocity vectors for each boundary layer, yields

$$\rho_t \mathbf{v}_t = \rho_b \mathbf{v}_b + \rho_n \mathbf{v}_n. \quad (21)$$

Here, the density of the band is the mass of band material in the whole volume, which is simply $\rho_b = a_b \rho_t$; likewise, the density of the non-bands is $\rho_n = (1 - a_b)\rho_t$ (assuming that the variations in densities due to differing melt fractions are negligible). Dividing by ρ_t, yields

$$\mathbf{v}_t = a_b \mathbf{v}_b + (1 - a_b)\mathbf{v}_n. \quad (22)$$

This vector equation is the source of all following constraints on the strain rates, as illustrated in Fig. 3.

Performing the following operations on this equation yields several constraints necessary for deriving relations between various components of the velocity gradient tensors.

(1) The divergence,

$$\nabla \cdot \mathbf{v}_t = \nabla \cdot [a_b \mathbf{v}_b + (1 - a_b)\mathbf{v}_n]$$
$$= a_b \nabla \cdot \mathbf{v}_b + (1 - a_b)\nabla \cdot \mathbf{v}_n \quad (23)$$

provides a relationship between dilatancy in the band and non-band regions. In these experiments, the samples are incompressible, such that $\nabla \cdot \mathbf{v}_t = 0$. This constraint is not used in the present analysis.

(2) The curl in the 1, 3 plane (the 'flow plane'),

$$\nabla \times \mathbf{v}_t = \nabla \times [a_b \mathbf{v}_b + (1 - a_b)\mathbf{v}_n]$$
$$= a\nabla \times \mathbf{v}_b + (1 - a_b)\nabla \times \mathbf{v}_n \quad (24)$$

gives a relationship between the shear strain rate in the band and that in the non-band regions discussed below.

Boundary conditions

The actual boundary conditions of the experiments are complicated; there is no change in total volume in the high-pressure experiments, but there is a small component of flattening and sidewards extrusion during shear (Holtzman *et al.*, 2003b). Thus, in the following approximations, the first is straightforward, but the second is a simplification of reality:

(1) The divergence of the flow must be zero, since no mass is gained or lost in the system:

$$\nabla \cdot \mathbf{v}_t = 0 \quad (25)$$

and so equation (23) gives

$$a_b(b_{11} + b_{33}) = -(1 - a_b)(n_{11} + n_{33}) \quad (26)$$

where $(b, n)_{i,j}$ refer to the components of the velocity gradient tensors for the bands and non-bands, respectively. This equation will be useful when the work done by compaction/dilation is considered. However, for the

rest of this paper, we assume that the shear deformation is much greater than the volumetric deformation (i.e. any ii components), and thus we neglect the volumetric terms altogether in this simplest approximation.

(2) The curl of the velocity field, equation (24), provides another relation between components of the velocity gradient tensors:

$$t_{13} = a_b(b_{13} - b_{31}) + (1 - a_b)(n_{13} - n_{31}). \quad (27)$$

We make the approximation that the gradients of velocity in the shear direction are also negligible, i.e. $b_{31} = n_{31} = 0$, so this equation becomes

$$a_b b_{13} + (1 - a_b)n_{13} = t_{13}. \quad (28)$$

Strain partitioning

Up to this point in this analysis the equations are symmetric in the sense that the bands and lenses are treated equally. Here, we introduce an asymmetry, an equation that prescribes the amount of strain partitioned into the bands, and a 'response' propagates into the strain rates in the lenses. In these experiments, the shear strain rate, $\dot{\gamma}_t$, is known, but the strain rates in the bands, $\dot{\gamma}_b$, and lenses, $\dot{\gamma}_n$, are not. Because these two unknown strain rates are coupled, we solve for $\dot{\gamma}_n$ in terms of $\dot{\gamma}_b$. Here, we define a partitioning factor, p_b, that relates the total shear strain rate to the shear strain rate in the bands. The definition of p_b includes the constraint that the shear strain rate in a band must be maximum when the band is parallel to the shear plane ($\alpha = 0$) and zero when it is parallel to the principle compressive stress, $\alpha = 45°$ in simple shear:

$$b_{13} = p_b t_{13} \cos(2\alpha). \quad (29)$$

In equation (29), the partitioning parameter

$$p_b = \left. \frac{b_{13}}{t_{13}} \right|_{\alpha=0} \quad (30)$$

is a factor describing the amount of strain rate partitioned into the bands, where $(b, t)_{ij}$ refer to the components of the velocity gradient tensors for the bands and the total, respectively. Equation (29) is analogous to Anderson's theory of faulting (Turcotte and Schubert, 1982, p. 354). The factor p_b embodies the principal unknown in this formulation. We substitute equation (29) into equation (28) for b_{13} and rearrange

$$n_{13} = \frac{t_{13}[1 - a_b p_b \cos(2\alpha)]}{(1 - a_b)}. \quad (31)$$

Thus, we have reduced all the components of the velocity gradient tensors to functions of t_{13} and p_b.

The evolution of p_b during melt segregation is one of the broader issues in this study. Because p_b is defined in terms of components of the velocity gradient tensor,

via the strain rates (see Appendix B), we can write p_b in terms of the constitutive relation for melt-bearing rocks, equation (19):

$$p_b = \frac{b_{13}}{t_{13}} = \exp\left[\lambda\phi_t(\phi_b - 1)\right]. \tag{32}$$

A path for p_b with increasing melt segregation can be written in terms of S_t, where $\phi_b = 1 + (\phi_{max} - 1)(S_t)^c$. In the solutions, we will compare the evolution of dissipation for paths of p_b as a function of S_t with three different values of c.

There is a clear physical limitation to the value of p_b. The vector diagram in Fig. 3c states that the velocity of any particle in the band (unweighted by a_b) cannot be larger than the velocity applied to the walls of the sample, that is, $|\mathbf{v}_b| \leq |\mathbf{v}_t|$. When this equality is solved, $|\mathbf{v}_b| = h_b b_{13}$ and $|\mathbf{v}_t| = h_t t_{13}$. When plugged in to the inequality statement and the substitutions made for

$$\frac{h_b}{h_t} = \frac{a_b}{\cos(\alpha)} \quad \text{and} \quad \frac{b_{13}}{t_{13}} = p_b\cos(2\alpha),$$

the result is a criterion that must be met for any combination of p_b and a_b:

$$a_b p_b \leq \frac{\cos(\alpha)}{\cos(2\alpha)}. \tag{33}$$

The result is plotted in Fig. 4. Values of $a_b p_b$ must lie below the solid curve in Fig. 4 for the dissipation calculation to satisfy the criterion $|\mathbf{v}_b| \leq |\mathbf{v}_t|$. This limit is ensured in the calculation by only solving dissipation for values of α for which the respective values of p_b and a_b satisfy these conditions.

The relationship between α and β

An interesting piece that falls out of these equations is the relationship between the angle of the band and non-band shear planes, or an expression for β in terms of only α, p_b and t_{13} (defined in Fig. 3). This relationship between α and β is derived in Appendix A and plotted in Fig. 5. There are several constraints on this relationship, which are also illustrated in Fig. 5:

(1) Based on crystallographic fabrics, when bands form at $\sim 20°$, the b-planes of olivine are rotated in the opposite sense away from the sample shear plane (i.e. the sample walls) by $\sim 20°$. The assumption that the b-planes are roughly parallel to the local 'non-band' shear plane is discussed in Holtzman et al. (2003b). Thus, we infer that when $\alpha \approx 20°$, then $\beta \approx -20°$.

(2) If the bands are parallel to the sample shear plane ($\alpha \approx 0°$), the shear plane in the melt-depleted lenses should also be parallel to the sample shear plane, so $\beta \approx 0°$.

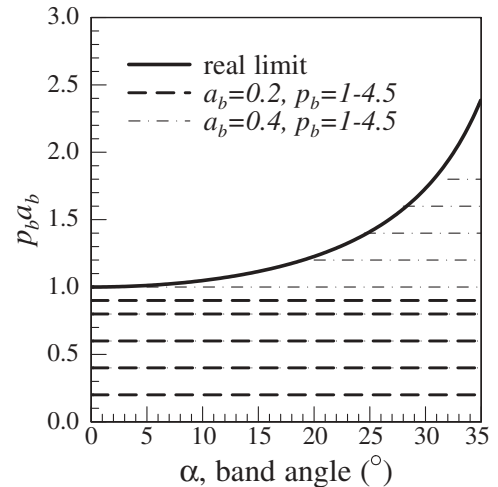(3) If the bands reached an angle of 45°, where they would be parallel to the maximum compressive stress,

Fig. 4. The limit of real solutions. This plot denotes the domain of real solutions to the analysis according to the limit derived in equation (33) and illustrated in Fig. 3d, for two values of a_b and ranges of p_b.
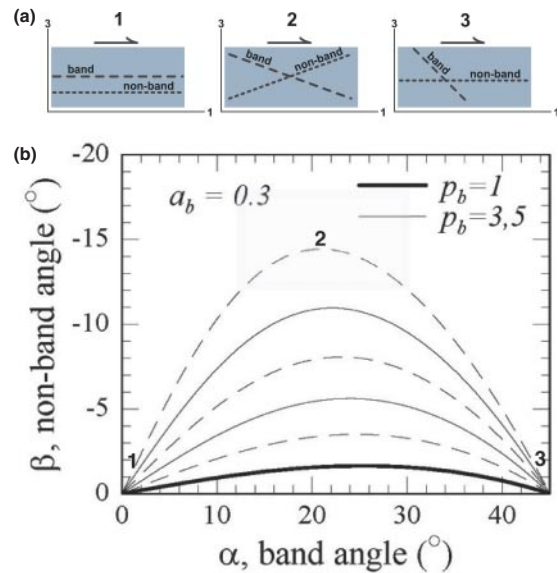

Fig. 5. The relations between α and β [see equation (52)]. (a) The relationship between these two reference frames is constrained by some data and some logic: (1) When bands are parallel to the reference (total) shear plane, so should be the shear plane in the non-band. (2) When bands are at an angle α to the shear plane, the non-band shear plane should also be at an angle β, back-rotated relative to the sense of shear, as observed in LPO data (Holtzman et al., 2003b). (3) When bands are parallel to the most compressive stress, $\alpha = 45°$, they cannot accommodate any shear, so the non-band angle should be 0. (b) Calculations of β as a function of α. The solid lines indicate odd values of p_b and the dashed lines indicate even values. The observed back-rotation of olivine b-planes of $\sim 20°$ is consistent with $p_b > 6$.

no shear stress is resolved on them such that they could only open in purely tensile mode. The shear in the non-band regions should then be parallel to the sample shear plane, such that when $\alpha \approx 45°$, $\beta \approx 0°$.

The theoretical predictions plotted in Fig. 5 match these three constraints very well. As discussed in the Appendix, this relationship is not needed to solve the strain rates because, in this version, we use only the (second) strain rate invariant, which, by definition is a scalar quantity derived from a tensor that is independent of orientation. However, we include the derivation here because it lends physical insight to the equations and may be useful in future modifications to the analysis.

Synthesis

The following array of equations comprise the analytical solution for the components of the strain rate tensor. The first two, derived in Appendix A, give the scalar second invariant of the strain rate tensor in the band and non-band regions. The second three were derived above:

$$
\begin{cases}
\dot{\boldsymbol{\varepsilon}}_{ij}^{b}\dot{\boldsymbol{\varepsilon}}_{ij}^{b} = \frac{1}{2}(b_{13})^2 & (a) \\
\dot{\boldsymbol{\varepsilon}}_{ij}^{n}\dot{\boldsymbol{\varepsilon}}_{ij}^{n} = \frac{1}{2}(n_{13})^2 & (b) \\
b_{13} = p_{b}t_{13}\cos(2\alpha) & (c) \\
n_{13} = \dfrac{t_{13}[1 - a_{b}p_{b}\cos(2\alpha)]}{(1 - a_{b})} & (d) \\
*p_{b} = \exp[\lambda\phi_{t}(\phi_{b} - 1)] & (e)
\end{cases}
\qquad (34)
$$

Again, the '*' indicates that this equation is only used when the equations are solved in terms of S_t and when p_b is not fixed. In this set of equations the constants are λ, ϕ_t, t_{13} and c. The dependent variables are $b_{13}(p_b, t_{13}, \alpha)$, $n_{13}(p_b, t_{13}, a_b, \alpha)$, $\beta(\alpha)$, and from equations (20), $\eta_{b,n}(S_t)$, $a_b(S_t)$ and $\phi_b(S_t)$. The independent variables are then α and S_t. We plot Φ_t as a function of α, initially treating a_b, ϕ_b and p_b as independent variables, and then all three as a function of S_t.

From the above equations we also calculate an approximate shear stress in the bands and lenses by using the following definition,

$$
\tau = \eta_{\phi}\sqrt{\dot{\boldsymbol{\varepsilon}}_{ij}\dot{\boldsymbol{\varepsilon}}_{ij}} = \eta_{\phi}\dot{\gamma}^{II}. \qquad (35)
$$

The difference between τ_b and τ_n,

$$
\Delta\tau_{b-n} = \eta_b\dot{\gamma}_b^{II} - \eta_n\dot{\gamma}_n^{II} \qquad (36)
$$

is a quantity with interesting implications for the dynamics of the melt band organization. However, the relationship of this stress (or stress difference) to the solid and melt pressure is discussed in much greater detail in Appendix C.

RESULTS

We solve equations (20) and (34) for total dissipation, Φ_t. In general, Φ_t develops a minimum at the band angle at which the contributions to the total from the bands and
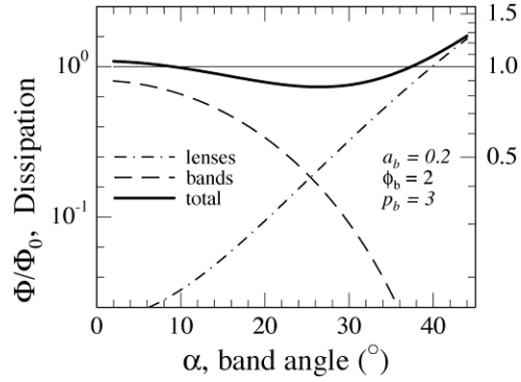

Fig. 6. The weighted contributions to the total dissipation from the bands and the non-bands. The minima in the total value develops where the two contributions cross over in magnitude. The horizontal solid line marks $\Phi/\Phi_0 = $ unity.

lenses are equal, that is, where dissipated energy is equipartitioned between the two regions, as shown in Fig. 6. The location of this minimum depends on a_b, ϕ_b and p_b. To develop these ideas we first illustrate the behavior of the equations by varying these parameters independently. Then, we present a more global picture of the behavior of the system as a function of the total segregation factor, S_t, which couples these parameters. We also demonstrate how the minimum in dissipation corresponds to the band angle at which shear stress is the same in the two regions.

In Fig. 6, the separate contributions (weighted by a_b) to Φ_t from the bands and the lenses are plotted as functions of α. The results are normalized by the reference dissipation for a material of the same total, but unsegregated, melt fraction, Φ_0. The bands and lenses make inverse contributions to the total dissipation. The band contribution is highest at low angles when the bands are well oriented to take up the largest amount of slip and lenses need to deform relatively little. As α increases, the contribution from the lenses increases because they have to deform more as the amount of deformation accommodated in the bands decreases. At the value of α where these contributions are equal in magnitude (α^*), that is, where energy is equipartitioned, a minimum exists in the total dissipation, defined where $(d\Phi/d\alpha)|_{p_b} = 0$ and $(d^2\Phi/d\alpha^2)|_{p_b} > 0$. In the following section, we explore how variations in each of the variables describing melt distribution, a_b and ϕ_b, influence the position of the minima in dissipation.

Dissipation, varying a_b and ϕ_b

In each panel of Fig. 7, Φ_t is plotted as a function of α with the partitioning factor p_b as the varied parameter. As discussed above, a minimum value of Φ_t occurs at α^* for a given value of p_b. For a given value of p_b, with
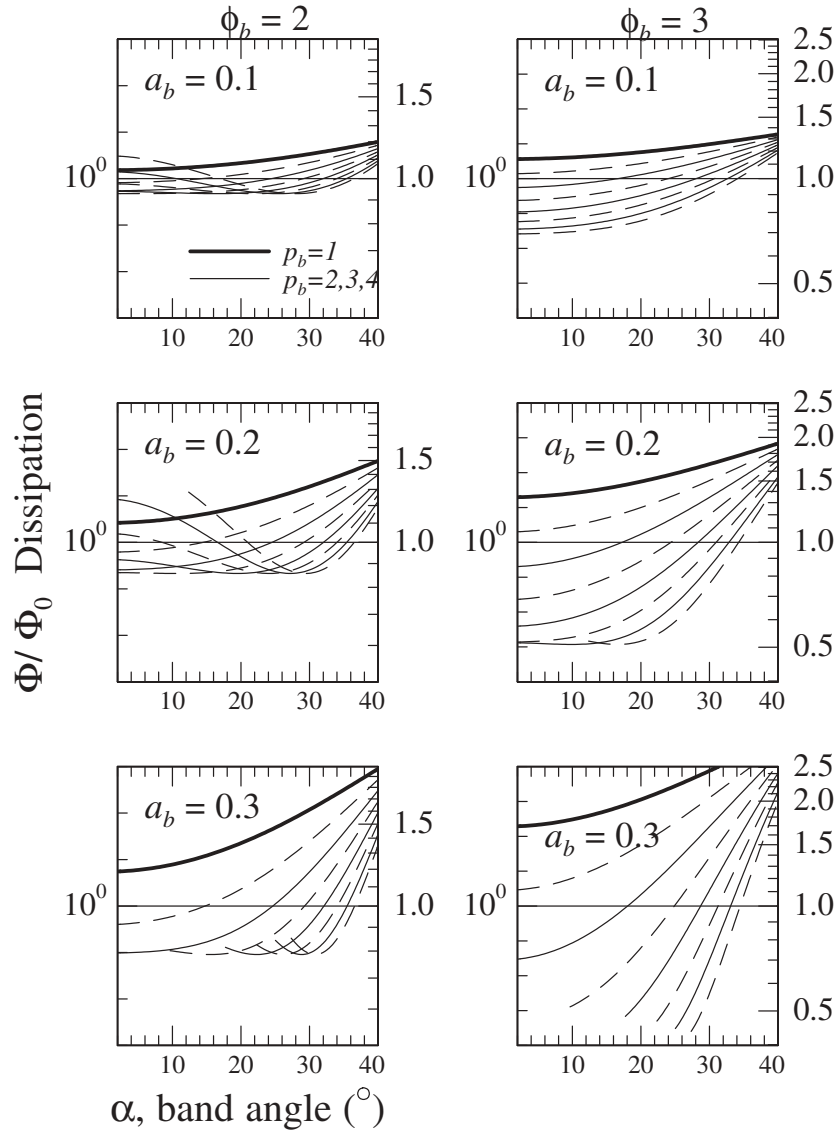
Fig. 7. Six plots of Φ_t as a function of α varying ϕ_b and a_b. Note the differences in locations of minima and absolute values of minima. Left column, $\phi_b = 2$; right column, $\phi_b = 3$. Reading left to right, then down, (a) $a_b = 0.1$, $\phi_b = 2$ and $S_t = 0.2$; (b) $a_b = 0.1$, $\phi_b = 3$ and $S_t = 0.3$; (c) $a_b = 0.2$, $\phi_b = 2$ and $S_t = 0.4$; (d) $a_b = 0.2$, $\phi_b = 3$ and $S_t = 0.6$; (e) $a_b = 0.3$, $\phi_b = 2$ and $S_t = 0.6$; (f) $a_b = 0.3$, $\phi_b = 3$ and $S_t = 0.9$. Note that in the lower left ($a_b = 0.3$ and $\phi_b = 2$), the curves are cut off just to the left of the minima, below which the solutions are not real, because they do not meet the criterion defined in equation (33). In the right column, with a higher value of ϕ_b (=3), the solutions with minima are fewer (because the criterion is met for fewer conditions), and where they exist, they occur at lower angles than for a smaller value of ϕ_b for a given value of p_b.

increasing α, dissipation decreases until a minimum is reached. As p_b values increase, these minima migrate towards higher values of α^*. Interestingly, for any fixed values of a_b, ϕ_b and λ, these minima all occur at the same value of Φ_t for all values of p_b. This situation occurs because, in this set of solutions, p_b is defined independently of a_b and ϕ_b. (In the 3D plots discussed below p_b does depend on a_b and ϕ_b.)

The six sets of $\Phi_t - \alpha$ curves plotted in Fig. 7 explore the effects of varying a_b and ϕ_b. The left and right columns illustrate the effects of increasing a_b when $\phi_b = 2$ and $\phi_b = 3$, respectively. In both columns, increasing the value of a_b results in greater reduction in dissipation (and greater spread between maximum and minimum values of Φ) and a higher value of α^* at the minimum in dissipation for a given value of p_b. In other words, p_b can be larger because the bands are much weaker owing to a higher melt fraction. In the right column, the magnitude of the reduction in dissipation is much greater, i.e. $\geq 50\%$, than in the left column. In Appendix D,

we describe in detail the dependence of Φ_t on variations in a_b, ϕ_b and p_b.

The evolution of dissipation with melt segregation

We can simplify the above results by coupling a_b, ϕ_b and p_b to the melt segregation parameter S_t, which is described by equations marked with a '*' in equations (20) and (34) [also (14), (15) and (32)]. In Fig. 8, various paths for the evolution of the a_b, ϕ_b and p_b are plotted as functions of S_t, which are parameterized only by the exponent c. From here on, Φ_t is calculated as a function of S_t and α, these producing a surface of Φ_t at different states. Figure 9a illustrates an example of one such surface for one set of paths with $c = 0.5$, as in Fig. 8. As S_t increases Φ_t gradually begins to decrease, and the tightness of the valley increases, i.e., the dependence of Φ_t on α strengthens. Thus, with increasing melt segregation and strain partitioning, the system tends to exert a stronger preference for a particular value of α^*.

In Fig. 10, top row, the 3D surface is reduced to 2D by contouring values of normalized dissipation. In these plots, as S_t increases along the x-axis, the contours tighten and the values of ϕ_t drop towards the minimum at α^*. The path of the minima with increasing S_t, shown by the gray dots, provides an easy means of visually comparing the effects of varying c. As c increases from 0.1 to 1, as shown in Fig. 8, the melt fraction in the bands is higher at any given value of S_t, consequently p_b is correspondingly higher and a_b is correspondingly lower. Therefore, ϕ_t tend to be lower, and α^* tends to be higher, in agreement with the results shown in Fig. 7.

Shear stress and the mean pressure difference, $\Delta\tau_{b-n}$

As discussed above, we can calculate the shear stress, τ, in the band and non-band regions, and $\Delta\tau_{b-n}$, to provide further insight into the meaning of the equations derived here. In Fig. 9b, τ in the bands and the non-bands is plotted as a function of α for the same path of a_b, ϕ_b and p_b as used in Fig. 9a. First, the shear stress in the bands is independent of S_t because p_b depends on ϕ_b such that shear strain rate increases proportionally to the decrease of viscosity in the bands as melt segregates. As α increases, the shear stress in the bands decreases, because the bands can accommodate less and less strain as they approach 45°. The stress in the lenses is more complicated, and depends on a_b and ϕ_b in addition to p_b.

For any value of S_t, the point where the two curves cross, that is, $\Delta\tau_{b-n} = 0$, corresponds to the band angle α^* at which Φ_t is minimized. In other words, the configuration at which dissipation is equipartitioned is also the set of conditions at which shear stress is uniform across
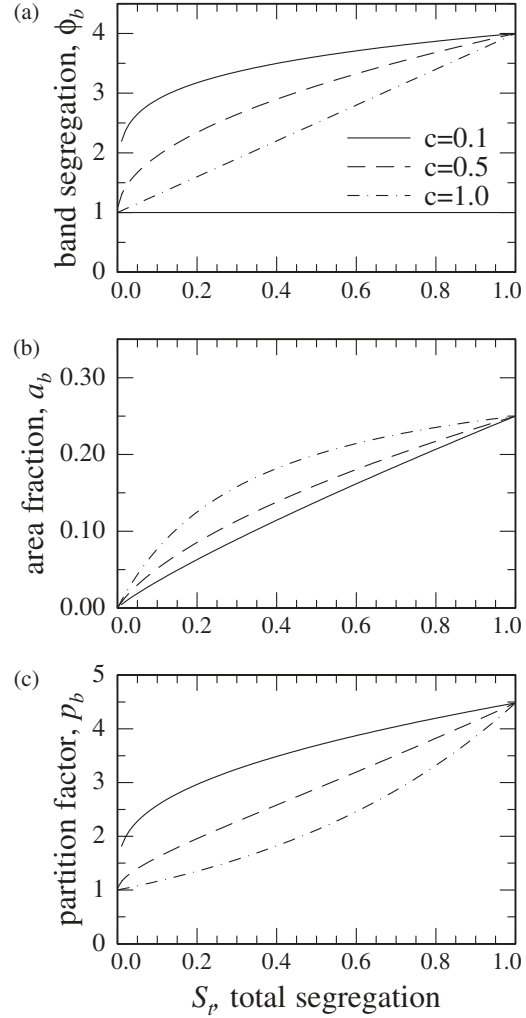

Fig. 8. The evolution of configurational parameters with increasing melt segregation, S_t, for $a_{max} = 0.25$, $\phi_{max} = 4$ and $c = 0.1$, 0.5, 1.0. (a) ϕ_b as a function of S_t; (b) a_b as a function of S_t; (c) p_b as a function of S_t.

the material, or [equation].

$$a_b\eta_b(\dot{\gamma}_b^{II}|_{\alpha*})^2 = (1 - a_b)\eta_n(\dot{\gamma}_n^{II}|_{\alpha*})^2 \quad (a)$$

$$\eta_b(\dot{\gamma}_b^{II}|_{\alpha*}) = \eta_n(\dot{\gamma}_n^{II}|_{\alpha*}) \quad (b)$$

$$\frac{\eta_b}{\eta_n} = \frac{(1 - a_b)(\dot{\gamma}_n^{II}|_{\alpha*})^2}{a_b(\dot{\gamma}_b^{II}|_{\alpha*})^2} = \frac{(\dot{\gamma}_n^{II}|_{\alpha*})}{(\dot{\gamma}_b^{II}|_{\alpha*})}. \quad (c) \qquad (37)$$

When viewed in 2D, as in the bottom row of Fig. 10, the line that describes the intersection of these two surfaces tracks perfectly the line of minimum dissipation. Because this line moves downward in τ with increasing S_t, the effective viscosity is decreasing (because the total strain rate is constant).

The fact that α^* corresponds to both the minima in Φ_t and the point where $\Delta\tau_{b-n} = 0$ has significant implications for the dynamics of the organization of the melt bands
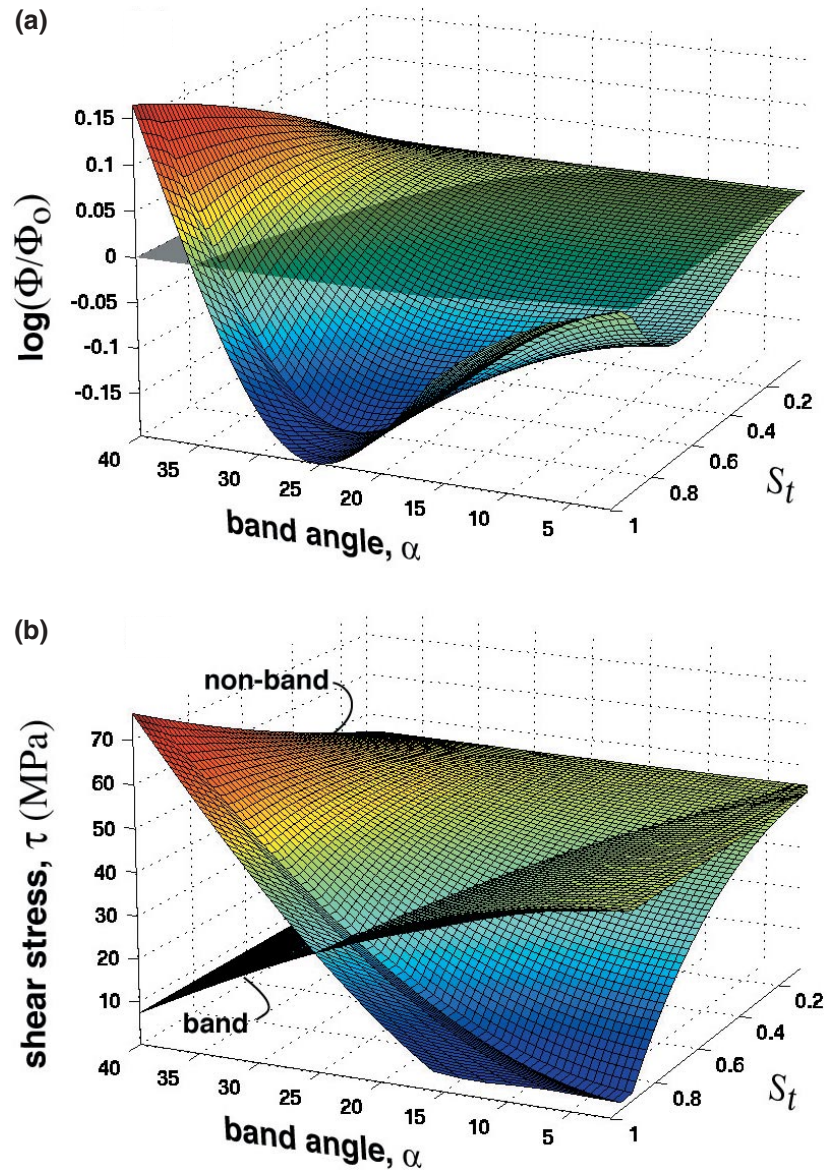
Fig. 9. 3D results of dissipation and shear stress calculations as a function of α and S_t. (a) log values of normalized dissipation as a function of α and S_t. p_b varies according to the path shown in Fig. 8 with $c = 0.5$, $a_{max} = 0.25$, $\phi_{max} = 4$ and $c = 0.5$. With increasing S_t, the value of α at Φ_{min} (α^*) increases up to $\sim$25°. (b) Shear stress, τ, as a function of α and S_t, for the same parameters as above. The surface for shear stress in the band is constant as a function of S_t because p_b varies with S_t such that shear stress is constant; as ϕ_b increases, strain rate increases inversely proportional to the viscosity decrease. However, strain rate varies a great deal in the non-band. In the bottom row of the following figure, the difference between these two surfaces ($\Delta\tau_{b-n}$) is plotted.

and the stability of the observed value of α. In the Discussion and Appendix C, we will explore this condition further in a speculative way, while not knowing the relationship between $\Delta\tau_{b-n}$, the pressure difference in the solid $\Delta\bar{P}_s^{b-n}$, and the pressure difference in the melt, ΔP_m^{b-n}.

Summary

(1) As ϕ_b and a_b increase, Φ_{min} decreases; as p_b increases, the angle at which Φ_{min} occurs, α^*, increases.

(2) As melt segregates (i.e. as S_t increases), the preference for a specific α^* becomes stronger (i.e. the potential wells become steeper). If ϕ_b, a_b and p_b increase roughly as described in Fig. 8, then α^* should increase as melt segregates, thus approaching an angle similar to those observed in experiments.

(3) At α^*, both Φ_{min} occurs and $\Delta\tau_{b-n} = 0$. An implication is that the bands may organize around an angle at which shear stress is constant in the sample and dissipated energy is minimized.
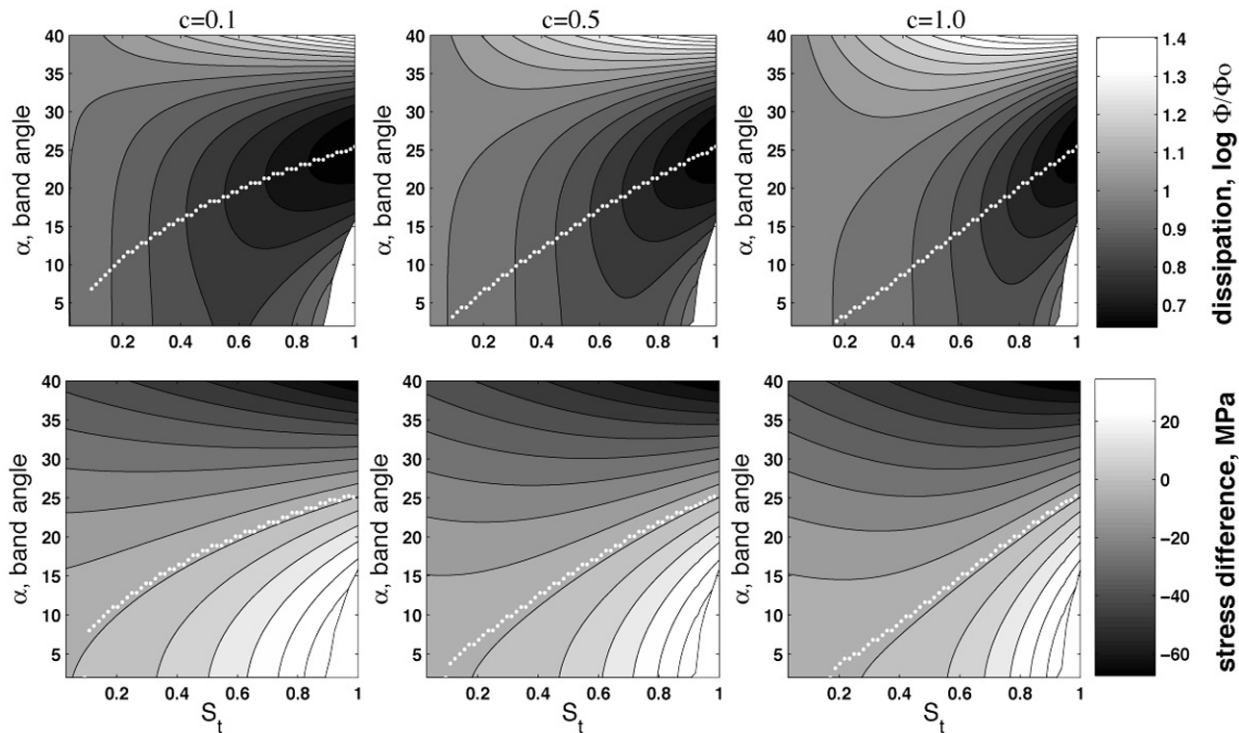
Fig. 10. The evolution of dissipation and shear stress difference with increasing melt segregation, S_t. These figures are the 2D equivalents of Fig. 9, where the z-axis values are contoured. The top row is the dissipation ($\Phi_t/\Phi_\circ$) and the bottom row is the shear stress (τ). Each column represents a different value of c, the exponent in the expressions for a_b, ϕ_b and p_b as functions of S_t. In each plot, the white dotted lines represent the values for α^* at Φ_{min} and $\Delta\tau^{b-n} = 0$. For each value of c, the paths of these lines are similar.

DISCUSSION

The above analysis is a partial description of the thermodynamics of melt segregation and strain partitioning, and is incomplete in several basic ways: (1) We look only at the steady state dissipation as a function of configurational parameters, but do not solve for growth or decay in these properties with time. (2) We do not incorporate length scales or statistics of melt distribution, only average properties of melt distribution. (3) Velocity fields are subject to very simplified constraints, in order to be solved analytically. (4) Viscosities are Newtonian. Nonetheless, the analysis captures some general trends in the changes of states of melt distribution and clues to the dynamics of the deforming system. It is intended to bridge experiments and fully dynamic numerical models and to provide a framework for analyzing and interpreting the experimental observations, written in terms of parameters that describe average properties (i.e. ϕ_b, a_b, α and Φ), which are directly measurable from experiments.

When dissipation is calculated as a function of the (coupled) degrees of melt segregation and strain partitioning, as well as the band angle, clear local and global minima develop. The implication is that, if a deforming system has the possibility of minimizing its energy dissipation or entropy production rate, it will tend in that direction. In the context of this analysis, variations in Φ_t can be viewed as small incremental movements between short-term steady states. The minimization at one value of S_t and transition to the next value of S_t occur by changing the melt distribution (band angle and melt content in bands) and strain partitioning such that the dissipated energy is equipartitioned between the bands and the lenses. The analysis predicts that the minima in dissipation can easily occur at the observed band angles. The main parameter that controls the value of α at which Φ_{min} occurs (α^*) is the degree of strain partitioning, p_b. However, in real (experimental and natural) systems, some other property of the system may influence the observed α, such as the ratio of shear to normal stress. The values of p_b may be closely coupled to spatial variations in dilation and compaction rates. In this analysis we do not explore such interplay.

We also demonstrate that the local minimum in dissipation corresponds to the equalization of stress and thus the elimination of stress gradients between the bands and the lenses. This finding is a more physically intuitive way of thinking about the stability of an average band angle in a constantly reorganizing melt-network; it leads to an answer to 'how?', whereas the energetics provides an answer to 'why?'. Below, we will develop an idea for how the system constantly readjusts melt distribution around

the optimal band angle, by a pumping mechanism driven by the departures from constant stress. Also, this tendency towards constant stress suggests that the 'Reuss bound' approximation of constant stress during strain partitioning is a good one, and will allow for the derivation of a much simpler set of equations that describe effective viscosity changes during melt segregation and strain partitioning.

The solutions provide several insights into the behavior of a deforming partially molten rock in which melt segregates and thus strain partitions. To illustrate these insights, first we describe this behavior in terms of the effect of strain partitioning on the total dissipation and begin to relate the conclusions to experimental observations. Second, we demonstrate simple inferences into the mechanics of melt segregation and self-organization of the networks of melt-rich bands. Finally, we discuss the implications of melt segregation and strain partitioning for the rheological properties of partially molten mantle and the irreversible thermodynamics of melt–rock interaction.

Relating theory and experimental observation: viscosity and dissipation

Magnitudes of dissipation change

In the data from the experiment shown in Fig. 2, viscosity is reduced by 30% as melt segregates and strain partitions, corresponding to a reduction in dissipation of 20%. For this sample, the value of S_t is ≈ 0.5. Thus, we have one point in the space described in Fig. 9, and it falls very close to the surface [at $S_t = 0.5$, $\alpha = 20°$ and $\Phi_t/\Phi_o = -0.1 = \log(0.8)$]. However, this result does not validate the analysis, but it is simply an illustration of how we will proceed in comparing the analysis to experimental data. Essentially, by measuring the parameters describing the melt distribution (a_b and ϕ_b, and thus S_t), α, and the final dissipation value, we can fit the data by varying the dependence of p_b on S_t.

The evolution of dissipation

The implication of the above paragraph is that the evolution of strain partitioning controls completely the evolution of dissipation. As shown in Fig. 2, within increasing strain, the dissipation (and the effective viscosity) decreases until about $\gamma = 1$, after which it flattens out. This flattening indicates that a steady state has been reached in the system, presumably in the statistical variations in the melt distribution and the strain partitioning. We suggest that the decrease in dissipation and effective viscosity is caused by an increase in strain partitioning, associated with increasing melt segregation. The onset of steady state may reflect the achievement of a balance between the processes of melt reorganization relative to the shearing solid and strain partitioning in the melt-rich
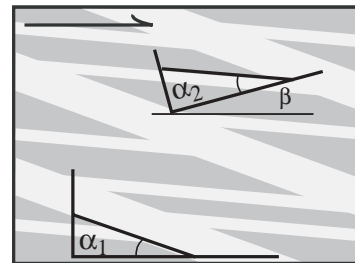

Fig. 11. Two scales of melt bands. The largest bands traverse the sample. The small bands connect the large bands at a lower angle relative to the shear plane. Here, we suggest that this pattern of melt distribution actually represents the same mechanical preference for a 15–20° angle at a second scale, i.e. in the lenses where the shear plane is back-rotated by β relative to the shear plane (i.e. $\alpha_1 \approx \alpha_2$). This would explain the bimodal distribution of band angles and the tendency of the lower angle bands to be narrower than high angle bands, as shown in Fig. 1.

network. As discussed below, the transition to steady state may coincide with an increased degree of connectedness of bands within the melt networks. When this connectivity increases, melt can redistribute and strain can partition more effectively than when bands are not connected; thus, the degree of connectedness and the potential for strain partitioning may be coupled.

Another aspect of the experiments not described in the analysis is the non-linear dependence of viscosity on stress. The degree of dislocation creep depends on stress and melt fraction (to the extent that melt fraction influences the effectiveness of grain boundary diffusion creep and also influences the grain size). As melt segregates, the stress magnitudes in the lenses will increase. Thus, in the right regime, the activity of dislocations may increase with melt segregation, causing weakening in the lenses. This weakening will couple to the deformation conditions in the band networks. These aspects can be quantified and accounted for in future versions of this analysis.

The melt distribution

In Fig. 1, the widest bands traverse the sample at higher angle relative to the shear plane than the thinner, more numerous bands. In the bimodal distribution of band angles, as shown in Figs 2b and 11, these wider bands constitute the smaller population of bands at higher angles. The narrow bands at lower angles connect the wider bands. We suggest that this pattern of band angle and thickness distribution is caused by the same set of processes occurring at a smaller scale; because of the strain partitioning, the stress field and thus the shear plane are back-rotated relative to the sense of shear by an angle of β, as illustrated in Fig. 11 and discussed in Holtzman *et al.* (2003b). In this view, the 'lower angles' actually have the same angle relative to their local shear plane as the thicker, higher angle bands do to the sample walls. Thus, the mechanical preference for a 15–20°

angle propagates downward in scale. This hypothesis explains the bimodal distribution of band angles. The lower angle bands tend to be narrower than high angle bands because they are forming in a region with lower background melt fraction. Another part of this story of the distribution of band angles involves rotation and growth of bands during shear, which is discussed below.

Mechanics of network formation and stability

Calculations of the dissipation do not reveal the mechanical process by which the system achieves any given state. However, when we look at the variations in stress between these two regions, as in Figs 9, 10 and 12, this simple picture of the variations in stress distribution with α explains qualitatively many aspects of the behavior of the networks during deformation. In the following, we discuss why bands nucleate, how networks form and maintain a dynamic steady state, and how they evolve. We want to understand how the melt moves through the sample, how these patterns of movement couple to the effective viscosity of the system, and ultimately how to extrapolate these dynamics to conditions in the Earth.

Why and how do bands nucleate and grow?

The notion of stress-driven melt segregation was first proposed by Stevenson (1989). In a 1D model of a deforming partially molten material, small perturbations in melt fraction cause small variations in viscosity because of the dependence of viscosity on melt fraction. In the limit where strain rate is spatially invariant, these low-viscosity regions are also low-pressure regions, so more melt tends to flow into them, leading to an instability, spontaneous melt segregation and band formation on length scales less than the compaction length, δ_c. Richardson (1998) extended the problem to 2D pure shear. None of these studies have been able to predict a characteristic spacing, other than that it will be less than a compaction length. Hall and Parmentier (2000) attempted to define a constraint on the band spacing by incorporating the effect of water removal during melting on increasing the matrix viscosity.

Rabinowicz and Vigneresse (2004) and Speigelman (2003) extended Stevenson's analysis to a simple shear boundary condition, in 1D and 2D, respectively. In a linear stability analysis, Spiegelman found that the melt segregation instabilities (bands) form at a range of angles and rotate with the shear flow and those at $\alpha = 45°$ grow fastest. In the linear analysis with Newtonian melt fraction-dependent viscosity, shear perturbations on the bands do not reduce rotation rate because they are not coupled to the background simple shear flow. Both Holtzman *et al.* (2003a) and Spiegelman (2003) suggested that the observed band angle is a compromise between
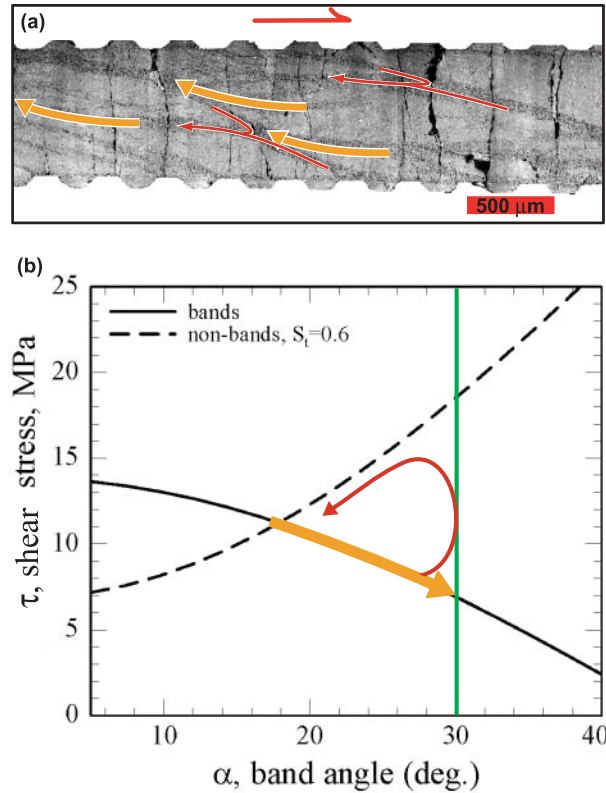

Fig. 12. Mechanics of the steady state: the melt 'pumping cycle'. (a) Melt must constantly be moving through the network for the average band angle to be constant. One hypothesis illustrated here is that melt is continuously pumped through the network, from low-angle bands to high-angle bands (thick orange arrows) and from high-angle bands to low-angle bands (thin red arrows) for the reasons illustrated below and discussed in the text. (b) A slice through Fig. 9b at $S_t = 0.6$. The two parts of the melt pumping cycle are illustrated with the same arrows as above. The thick orange arrow represents the driving force for melt to migrate from low angle to high angle bands because their shear stress, and thus their mean pressure, is lower. The red arrow implies that at some critical angle, the melt pressure increases to be closer to that of the stress in the lenses; this causes a flip in the direction of the melt pressure gradient, driving melt from bands at high to low angles. The cause of this change in melt pressure is the increased deformation in the lenses squeezing melt-rich bands together and raising the melt pressure. The green (vertical) line represents the maximum angle at which bands are observed.

the fastest growing orientation (45°) and the orientation of maximum shear (0°). In this analysis, consideration of strain partitioning and not growth rate leads us to a different, but not necessarily exclusive, conclusion.

Here, we directly couple the flows in the band and non-band regions, but are limited to assuming a steady state; however, we can speculate on the conditions that cause the initial segregation of melt, using the illustration in Fig. 12. In the plot of τ as a function of α, to the right of α^*, at which $\Delta\tau^{b-n} = 0$ (i.e. the crossover of the $\tau(\alpha)$ curves for the band and the non-band), melt flows down the pressure gradient, from non-band to band regions. This curve implies that, as bands rotate with increasing

shear strain to higher angles, melt flows from bands at low angle to ones at high angle, consistent with the (instantaneous) observed correlation between band angle and thickness, and with the results of Speigelman (2003). The value of α^* depends on S_t and p_b, so bands should be observed at angles equal to or less than α^*, where the condition for the growth of bands is met. However, they tend to rotate to higher angles, up to an observed limit of ~30° not 45°, as discussed below. An attempt to explain this upper limit is made below. The existence of bands at lower angles than α^* may be explained by the strain partitioning and multiple scales of segregation, as discussed above and in Fig. 11.

How is a steady state maintained?

As discussed in Holtzman *et al.* (2003a), in order to maintain a steady state and a constant average band angle, melt must constantly move relative to the solid. The following hypothesis is based on the analysis, but is an inference based more on the observations than the calculations. We propose that the steady state average band angle is maintained by the following 'pumping' cycle, illustrated in Fig. 12:

(1) Bands nucleate by the mechanism discussed above at some low value of α.

(2) As a band rotates with the overall shear flow, it grows (i.e. melt fraction and thickness increase) up to a limit, which is observed at ~30°. The orange arrow in Fig. 12a shows melt flowing from a band at low angle to one at slightly higher angle. In Fig. 12b, this flow is represented by the orange arrow that tracks the decreasing shear stress in the band with increasing band angle.

(3) An upper limit of the band angle ($\approx$30°) is reached at which melt is driven back to lower angle bands, as shown by the red arrows in Fig. 12a and b. The upper limit of band angles exists because the system will only tolerate a certain shear or mean stress difference between the bands and non-band regions. As the bands rotate to higher angle, the lenses are forced to deform at higher rates, increasing the stress in them, as plotted in Fig 12b. As they deform more, they squeeze the bands, increasing the stress in the solid framework in a band, thus increasing the melt pressure in the bands. This increased melt pressure drives melt from high to low angle bands. The red arrow in Fig. 12b moves from the shear stress in the band to that in the lens, representing the local increase in stress as a band at high angle starts to be squeezed between two lenses. This change in stress does not fall out of the analysis because we only consider the simple shear components of deformation. Thus, this idea is testable in theory by calculating the flattening components of the solid deformation in the lenses, and coupling these modes to the stress in the band. The key to the pumping mechanism is that the slope of the shear stress gradient with band angle switches from negative (orange line) to positive (red).

This pumping cycle drives a net melt flow relative to the solid through the network of melt-rich bands, such that the average band angle remains constant as the sample deforms in shear. This process relies on the existence of a highly connected network, as observed in experiments (Figs 1 and 2) and illustrated in Fig. 11.

Another mechanism and pathway by which melt migrates relative to the solid may exist, as proposed by Holtzman *et al.* (2003a). In this mechanism referred to as 'wave migration', the melt in a band migrates against the solid flow by doing work against the solid to open porosity on the 'upstream' side and close porosity on the 'downstream' side, moving as a wave of porosity through the solid matrix. This process does not require the presence of a network; every band struggles on its own.

The variations in the evolution of Φ with increasing strain may represent variations in the dominant mechanism by which bands are moving relative to the solid. We propose that the energetics of the two band migration mechanisms actually differ, although this point is not considered in the analysis. The wave migration mechanism may both consume more energy (i.e. make η_{eff} higher) in the opening and closing of melt pockets and partition strain less effectively than a network can. The network migration requires longer distances of melt travel than wave migration, but these pathways have much higher permeability than non-band regions. Both mechanisms may occur at different locations in the network at any given moment and/or time. If the energetics of the two mechanisms are significantly different, the initial increase in effective viscosity in some experiments (not shown) may indicate a dominance of the wave migration mechanism over the network migration mechanism at the start of an experiment, before the connected network develops. If so, the decrease in η_{eff} with increasing strain results from a subsequent increase in the effectiveness of the mechanism of network migration.

Implications for the Earth

Increasingly, we are able to quantitatively study partially molten regions in the Earth as complete dynamic and thermodynamic system. In this view, the formation and persistence of melt-rich networks will characterize the close coupling between dynamics of mantle flow and thermodynamics of melting. However, for now, we separate the discussion into implications for rheological properties and for melting thermodynamics.

Rheological properties

When strain partitioning in networks occurs, the macroscopic effective rheological properties reflect mesoscopic variations in viscosity as well as the microscopic

deformation mechanisms that determine those viscosities. Thus, to determine these effective rheological properties (i.e. η_{eff}) constitutive equations must be written in terms of the geometric and rheologic properties of the various regions combined in a physically meaningful way. Most simply, $\eta_{eff} = \Phi_t/(\dot{\gamma}_t)^2$, where Φ is calculated with equations (20) and (44). Although we made some progress towards this aim, this approach is probably limited. Since the assumption of constant stress appears to be a good one, deriving an effective viscosity from a Reuss-bound calculation will be useful.

As discussed above, in the tightly confined conditions of our experiments the reduction of dissipation (or effective viscosity) is less than an order of magnitude. The effective viscosity for reasonable earth-like values of many of the parameters for a segregated system (1.8×10^{18} Pa.s) gives a 50% reduction of the melt-present viscosity (3.7×10^{18} Pa.s for $\phi_t = 0.04$), that is, an almost order-of-magnitude reduction of the melt-free viscosity (1×10^{19} Pa.s). However, in natural systems with less rigid boundaries (and boundary conditions) than in the experiments, systems may have more degrees of freedom to organize into configurations that allow greater reductions in viscosity.

Thermodynamics of melting and melt–rock reaction

The formation of melt-rich networks and the onset of strain partitioning have interesting implications for the thermodynamics of melt formation and extraction processes. Both deformation due to mantle flow and melt transport in networks can influence the entropy budget, as stated by the relation between energy and entropy in equation (3). The very fast and effective segregation and transport of melt provided by the network will lead to both positive and negative contributions to the energetics of melt–rock reaction. Asimow (2002) expanded the energy equation of McKenzie (1984, equation A37) to include the irreversible terms and the energy contributions of melt–solid disequilibrium in addition to the enthalpy of isentropic decompression. In his scaling analysis, Asimow compares the energies of all irreversible terms to the energy available to drive melting due to adiabatic (isentropic) decompression, or the enthalpy ΔH. This value is $\rho W C_p(\partial T/\partial z) \approx 3 \times 10^{-6}$ W/m^3 where ρ is the density (3.3×10^3 kg/m^3), W is the upwelling velocity ($\approx 10^{-1}$ m/year), C_p is the isobaric heat capacity [≈ 1000 J/(K.kg)] and $(\partial T/\partial z)$ is the geotherm (≈ 0.3 K/km). He isolates these irreversible contributions as the (1) thermal conduction and radiogenic heat production; (2) viscous dissipation in the fluid due to buoyancy driven compaction (including gravitational energy release and frictional heating); (3) viscous dissipation in the matrix as a result of compaction; (4) advection of heat by migrating melt; and (5) compositional disequilibrium
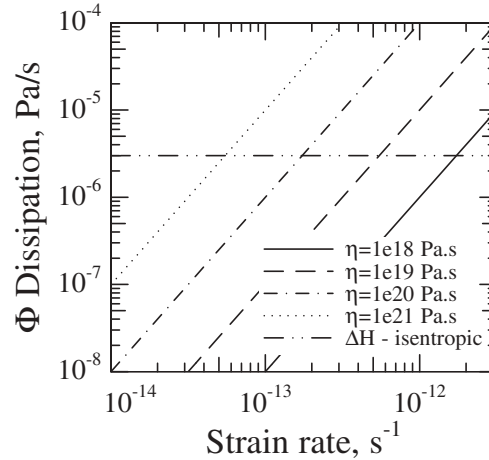

Fig. 13. Is viscous dissipation an important contribution to the energy available to cause melting of the mantle? The dissipation values for a range of normal strain rates and upper mantle viscosities, compared with the power per unit volume available to cause melting, $\Delta H_{isentropic}$, after Asimow (2002). The reduction of dissipation caused by strain partitioning will lower each of these curves by up to an order of magnitude.

between solid and melt. In the following discussion, we address the influence of the formation of melt-rich connected networks on several of these contributions. For the sake of discussion, we assume that stress-driven networks form deep in the melting column, and other melt transport/segregation mechanisms occur subsequently. To explore that assumption, a greater understanding of the relative kinetics of stress-driven and reaction-driven segregation is required, as discussed further below.

Deformation and dissipation. Asimow's analysis examines viscous dissipation in the migrating melt and solid due to compaction. He concludes that both of these terms are insignificant. However, the contribution to the total dissipation may be much greater from the shear deformation than from compaction. Because his analysis is 1D, Asimow does not include deformation due to corner flow. As shown in Fig. 13, the dissipation has a wide range of values for reasonable mantle strain rates and effective viscosities beneath a mid-ocean ridge; these values broadly straddle isentropic decompression value for power available to drive melting, implying that, in some locations, the heat produced by dissipation may contribute to melting.

As illustrated in Fig. 14, for perfectly passive upwelling, the stress, strain rate and thus the dissipation will be zero in the center and will increase towards the flanks of the melting region, with maximum values in the region of tightest corner flow for the case of a Newtonian viscous flow. Dissipation will be highest where stresses are highest in a slab-pull-driven spreading center, where a constant global strain rate is imposed. If equipartitioning and minimization of dissipation are achieved, then the
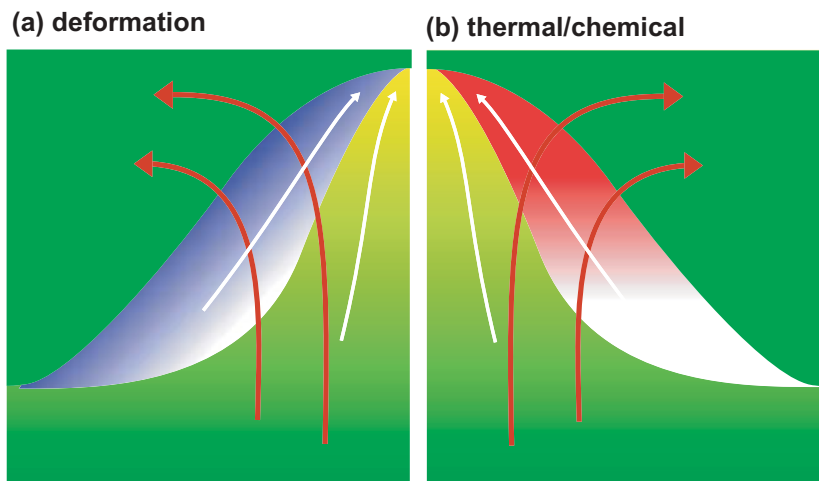
(a) deformation   (b) thermal/chemical

Fig. 14. A schematic illustration of the effects of stress-driven melt segregation and transport on thermodynamics of melting and melt-rock reaction beneath a ridge. In both figures, red lines indicate the mantle flow paths and white lines indicate melt flow paths. (a) The white-to-blue region indicates where dissipation will be relatively high, and the gradient represents increasing levels of stress, which should be mirrored in degree of stress-driven melt segregation (S_t), and the increase in permeability with network formation. (b) The white-to-red gradient indicates a transition from net reduction in entropy due to efficient melt extraction and thus the most fractional melting (white) towards a net increase in entropy due to the advection of heat and chemical disequilibrium from deeper levels.

entropy production would be reduced relative to that of a homogeneously deforming system. However, this reduction may still leave the dissipation large enough to contribute considerably to the total energy of the system available to drive melting. For example, for $\eta = 1 \times 10^{19}$ Pa.s and $\dot{\gamma} = 5 \times 10^{-13}$ l/s, $\Phi = 2.5 \times 10^{-6}$ Pa/s, or 83% of ΔH due to upwelling. A 50% reduction in η due to melt segregation would cause a 50% reduction in Φ or 42% of ΔH.

Melting and melt–rock reaction. The effects of stress-driven segregation on the transport properties of a partially molten region may tend to increase the disequilibrium and the irreversible contributions to the total energy. Continuing with the mid-ocean ridge example, we offer the hypothesis that melting may be more 'batch'-like in the center of the melting column where stresses are lower and stress-driven segregation is less effective, and more 'fractional' at the flanks of the melting region, where stress drives melt segregation more efficiently. When melt segregates easily at small melt fractions, the melting is more fractional than batch-like in nature. Fractional melting generally leads to lower melt productivity than a batch melting model in which the melt has time to equilibrate with its source (Asimow *et al.*, 1997). The degree of fractional melting will depend on the relative kinetics of the stress-driven and reaction-driven mechanisms. Estimating these kinetics is beyond the scope of this paper. As illustrated in Fig. 14, the compositional lithosphere (dark green) forms where enough water, Fe and melt have been extracted that the remaining rock is significantly stronger than adjacent asthenosphere material (Hirth and

Kohlstedt, 1996; Phipps Morgan, 1997). In this idea, much of the upwelling peridotite will pass through a region of more batch-like melting followed by more fractional melting in regions where segregation is driven by stress. Both Kelemen *et al.* (1997) and Asimow (1999) concluded that most parcels of melting peridotite have to undergo part of their melting history in a batch melting mode and part in a fractional melting mode, but placed no constraints on the spatial or temporal sequence. We would predict that the fractional melting follows an initial period of batch melting.

In more detail, we also suggest further spatial variations in the melting thermodynamics. Fast and efficient melt segregation by stress-driven network formation in the deep parts of the melting region will lead to greater melt–rock disequilibrium at shallower levels in the melting region. A highly connected network allows fast melt transport to advect heat upward and to cause greater differences in chemical potentials between melt and solid, thus contributing more energy to the melt–rock reactions at shallower levels in the melting region. These reactions lead to an instability called the 'reaction infiltration instability' (RII) (Aharonov *et al.*, 1995; Daines and Kohlstedt, 1993). This mechanism can cause efficient melt segregation, channel formation and transport, but requires initial melt–rock disequilibrium and subsequent dissolution in order to occur. As melt is quickly segregated and chemically isolated from its source rock, the degree of melt–rock disequilibrium increases as the melt ascends, thus increasing the efficiency of the RII as a mechanism of channel formation. The greater the degree of disequilibrium between melt and peridotite, the more

rapid will be the dissolution reaction kinetics that produce dunite from peridotite. Thus, stress-driven and dissolution driven melt segregation mechanisms will probably interact closely in the mantle. In this scenario, the RII may be more efficient at shallower levels in the melting column and may act to stabilize channels formed by stress-driven melt segregation.

In conclusion, there may be large spatial variability in the controls on the thermodynamics of melting beneath a ridge and other melting, deforming regions in the Earth. Where stresses are low, melting may be more batch-like, and thus productivity will be higher. As stresses increase, stress-driven segregation causes more fractional melting, implying lower productivity. However, in these regions, both the dissipation due to deformation and the increasing thermal and chemical disequilibrium may lead to increased productivity. Thus, it is possible that these two opposite trends will tend to balance each other such that an isentropic approximation would be reasonable. This conjecture can be explored quantitatively in further studies.

CONCLUSIONS AND FURTHER QUESTIONS

Although simple, this analysis provides insight into a possible mechanism by which networks of melt-rich bands form and maintain an average configuration in a dynamic steady state, by achieving an equipartition of energy dissipation between melt-rich and melt-poor regions. The values of energy dissipation in the partitioned system are very sensitive to several parameters that characterize the melt distribution, and these predictions can be compared quantitatively with experimental observations. Numerous variations could be added to this analysis, but we present it here in its skeletal form. The success it has when compared with experimental data will determine which modifications are made. However, several possible directions are worth pointing out for their value in describing unanswered questions.

(1) *Compaction and decompaction*. In the analysis above, we assume that the simple shear velocity gradient contributes far more to the total viscous energy dissipation than the work done in accommodating local changes in melt fraction (i.e. compaction and decompaction). Though the paths along which melt flows are not solved explicitly (i.e. the compaction equations are not solved), the volumetric change may be accounted for in the energy lost in changing the melt fraction, as the bands migrate relative to the solid. To maintain stability, the bands must constantly be adjusting. To adjust, they must be able to do work against the solid matrix. If we can estimate the driving force for local melt migration, then we can constrain the ability of the solid to resist decompaction,

that is, the bulk viscosity. Including these terms may modify the preference for an angle associated with a certain degree of strain partitioning.

(2) *Length scales and statistical distribution of melt*. At present, the analysis is written in very simple average boundary layer approximations with no coupling on interfaces between the boundary layers. However, deforming systems with identical average properties may have different local distributions of melt. Will the energy dissipation of a system with one band of area fraction *a* equal that of a system with 10 bands of 0.1*a*? If not (as seems likely), we need to incorporate the spacings between bands and mechanical interactions between band and non-band regions at their interfaces.

(3) *The need for non-linear dynamic models*. A complete continuum mechanical description of a melt-segregation process requires coupled mass, momentum, and energy conservation equations for two fluids with very different rheological properties (McKenzie, 1984; Scott and Stevenson, 1984; Fowler, 1990; Bercovici *et al.*, 2001). The viscoelastic properties of the matrix are generally, though not always (Connolly and Podladchikov, 1998) ignored, but may be important. Non-linear solutions arise because of the dependence of both permeability and viscosity on melt fraction, as well as the effects of stress-dependent viscosity. We must seek the simplest theory that can describe the full richness of behavior exhibited in experiments. Fully dynamic models will be an essential part of extrapolating the experimental results to natural settings.

Ultimately, we aim to be able to map S_t onto partially molten regions of the Earth, in spatial and temporal variations. Knowing the degree of melt segregation and all the related parameters, we can constrain the effects of meso-scale self-organization of melt on the rheological, seismic and transport properties of these regions. By calculating seismic properties (anisotropy and attenuation) directly to S_t, direct comparisons of model and observation may be possible.

REFERENCES

Aharonov, E., Whitehead, J. A., Kelemen, P. B. & Spiegelman, M. (1995). Channeling instability of upwelling melt in the mantle. *Journal of Geophysical Research* **100**, 20433–20450.

Asimow, P. D., Hirschmann, M. M. & Stolper, E. M. (1997). An analysis of variations in isentropic melt productivity. *Philosophical Transactions of the Royal Society of London, Series A* **355**, 255–281.

Asimow, P. D. (1999). A model that reconciles major- and trace-element data from abyssal peridotites. *Earth and Planetary Science Letters* **169**, 303–319.

Asimow, P. D. (2002). Steady-state mantle–melt interactions in one dimension: II. Thermal interactions and irreversible terms. *Journal of Petrology* **43**, 1707–1724.

Batchelor, G. K. (1967). *An Introduction to Fluid Mechanics.* Cambridge University Press, Cambridge, 615 pp.

Bercovici, D. & Ricard, Y. (2003). Energetics of a two-phase model of lithospheric damage, shear localization and plate-boundary formation. *Geophysical Journal International* **152**, 581–596.

Buck, R. & Su, W. (1989). Focused mantle upwelling below mid-ocean ridges due to feedback between viscosity and melting. *Geophysical Research Letters* **16**, 641–644.

Connolly, J. A. D. & Podladchikov, Y. Y. (1998). Compaction-driven fluid flow in viscoelastic rock. *Geodinamica Acta* **11**, 55–84.

Conrad, C. P. & Hager, B. H. (1999). Effects of plate bending and fault strength at subduction zones on plate dynamics. *Journal of Geophysical Research* **104**, 17551–17571.

Cooper, R. (1990). Differential stress induced melt migration: an experimental approach. *Journal of Geophysical Research* **95**, 6979–6992.

Daines, M. J. & Kohlstedt, D. L. (1993). A laboratory study of melt migration. *Philosophical Transactions of the Royal Society of London* **342**, 43–52.

de Groot, S. R. & Mazur, P. (1984). *Non-equilibrium Thermodynamics.* Dover, New York, 510 pp.

Fowler, A. C. (1990). A compaction model for melt transport in the earth's asthenosphere. Part I: the basic model. In: Ryan, M. P. (ed.) *Magma Transport and Storage.* John Wiley & Sons, New York, pp. 4–14.

Froideveaux, C. (1973). Energy dissipation and geometric structure at plate spreading boundaries. *Earth and Planetary Science Letters* **20**, 419–424.

Hall, C. E. & Parmentier, E. M. (2000). Spontaneous melt localization in a deforming solid with viscosity variations due to water weakening. *Geophysical Research Letters* **27**, 9–12.

Holtzman, B. K., Groebner, N. J., Zimmerman, M. E., Ginsberg, S. B. & Kohlstedt, D. L. (2003). Stress-driven melt segregation in partially molten rocks. *Geochemistry, Geophysics, Geosystems* **4**, 8607.

Holtzman, B. K., Kohlstedt, D. L., Zimmerman, M. E., Heidelbach, F., Hiraga, T. & Hustoft, J. (2003). Melt segregation and strain partitioning: implications for seismic anisotropy and mantle flow. *Science* **301**, 1227–1230.

Hirth, G. & Kohlstedt, D. L. (1996). Water in the oceanic upper mantle: implications for rheology, melt extraction and the evolution of the lithosphere. *Earth and Planetary Science Letters* **144**, 93–108.

Kameyama, M., Yuen, D. A. & Fujimoto, H. (1997). The interaction of viscous heating with grain-size dependent rheology in the formation of localized slip zones. *Geophysical Research Letters* **24**, 2523.

Kelemen, P. B., Shimizu, N. & Salters, V. J. M. (1995). Extraction of mid-ocean-ridge basalt from the upwelling mantle by focused flow of melt in dunite channels. *Nature* **375**, 747–753.

Kelemen, P. B., Hirth, G., Shimizu, N., Spiegelman, M. & Dick, H. J. B. (1997). A review of melt migration processes in the adiabatically upwelling mantle beneath oceanic spreading ridges. *Philosophical Transactions of the Royal Society of London, Series A* **355**, 283–318.

Mase, G. (1970). *Theory and Problems of Continuum Mechanics.* McGraw-Hill, New York.

McKenzie, D. (1984). The generation and compaction of partially molten rock. *Journal of Petrology* **25**, 713–765.

Mei, S., Bai, W., Hiraga, T. & Kohlstedt, D. (2002). Influence of melt on the creep behavior of olivine-basalt aggregates under hydrous conditions. *Earth and Planetary Science Letters* **201**, 491–507.

Nicolis, G. & Prigogine, I. (1977). *Self-organization in Nonequilibrium Systems.* John Wiley & Sons, New York.

Phipps Morgan, J. (1997). The generation of a compositional lithosphere by mid-ocean ridge melting and its effect on subsequent off-axis hotspot upwelling and melting. *Earth and Planetary Science Letters* **146**, 213–232.

Rabinowicz, M. & Vigneresse, J.-L. (2004). Melt segregation under compaction and shear channelling: application to granitic magma segregation in a continental crust. *Journal of Geophysical Research* **109**, 4407.

Ranalli, G. (1995). *Rheology of the Earth.* Kluwer Academic, Dordrecht, 432 pp.

Richardson, C. N. (1998). Melt flow in a variable viscosity matrix. *Geophysical Research Letters* **25**, 1099–1102.

Scott, D. R. & Stevenson, D. J. (1986). Magma ascent by porous flow. *Journal of Geophysical Research* **91**, 9283–9296.

Spiegelman, M. (2003). Linear analysis of melt band formation by simple shear. *Geochemistry, Geophysics, Geosystems* **4**, 10.1029/2002GC000499.

Stevenson, D. J. (1986). On the role of surface tension in the migration of melts and fluids. *Geophysical Research Letters* **13**, 1149–1152.

Stevenson, D. J. (1989). Spontaneous small-scale melt segregation in partial melts undergoing deformation. *Geophysical Research Letters* **16**, 1067–1070.

Turcotte, D. & Schubert, G. (1982). *Geodynamics.* John Wiley & Sons, New York.

Yuen, D. & Schubert, G. (1977). Athenospheric shear flow: thermally stable or unstable? *Geophysical Research Letters* **4**, 503–505.

Zimmerman, M. E. & Kohlstedt, D. L. (2004). Rheological properties of partially molten lherzolite. *Journal of Petrology* **45**, 275–298.

APPENDIX A: VELOCITY GRADIENT TENSORS

Here, we solve for the velocity gradient and strain rate tensors in the bands and non-bands by using the reference frames shown in Fig. 3. In the experimentally deformed samples, the deformation is 3D (Holtzman *et al.*, 2003b), and thus there are no null components of the strain rate tensor. However, for simplicity as discussed above, we assume that the dominant components of the tensor are the 13 components (i.e. $b_{31} = n_{31} = 0$), simplifying the problem to 2D. We further reduce these tensors to only their 13 components, prior to rotation, based on the assumption that the local shear (13) components are much greater than any dilatational (ii) components. Therefore,

$$\mathbf{B} = \begin{bmatrix} 0 & b_{13} \\ 0 & 0 \end{bmatrix}, \quad \mathbf{N} = \begin{bmatrix} 0 & n_{13} \\ 0 & 0 \end{bmatrix}, \quad \mathbf{T} = \begin{bmatrix} 0 & t_{13} \\ 0 & 0 \end{bmatrix} \tag{38}$$

where $b_{13} = (\partial v_1/\partial x_3)_b$, $n_{13} = (\partial v_1/\partial x_3)_n$ and $t_{13} = (\partial v_1/\partial x_3)_t$. The band and non-band velocity gradient tensors are then rotated into the sample (t) reference frame, using the rotation tensor

$$\mathbf{R} = \begin{bmatrix} \cos\theta & \sin\theta \\ -\sin\theta & \cos\theta \end{bmatrix} \qquad (39)$$

where $\theta = \alpha$ or β. [In 3D, this rotation occurs about the two-axis, normal to the shear direction (1), in the shear plane (1–2)]. The rotated matrix is calculated as, for example,

$$\mathbf{B}^R = \mathbf{R}\mathbf{B}\mathbf{R}^T. \qquad (40)$$

The band angle α is >0 and the non-band angle β is <0, as counterclockwise angles are positive. The velocity gradient tensor must first be rotated into the total (sample) reference frame and then decomposed into the strain rate form. (These operations are not dependent on the order in which they are performed.) The following derivation is for the strain rate in the bands; the exact parallel method applies for the non-bands.

The solution for the velocity gradient tensor in the band, rotated into the sample reference frame, is

$$\mathbf{B^R} = \begin{bmatrix} b_{13}\sin\alpha\cos\alpha & b_{13}\cos^2\alpha \\ -b_{13}\sin^2\alpha & -b_{13}\sin\alpha\cos\alpha \end{bmatrix}. \qquad (41)$$

To calculate the strain rates, these tensors are decomposed into a deformation part, the strain rate, $[(\partial v_i/\partial x_j) + (\partial v_j/\partial x_i)]$ and a rotational part, the vorticity, $[(\partial v_i/\partial x_j) - (\partial v_j/\partial x_i)]$ (Mase, 1970, p. 112), such that

$$\dot{\varepsilon}_{ij}^b = \frac{1}{2}\left[\mathbf{B^R} + (\mathbf{B^R})^T\right] \qquad (42)$$

where T indicates 'transpose'. We are mainly interested in the strain rate tensor,

$$\dot{\varepsilon}_{ij}^b = \frac{1}{2}b_{13}\begin{bmatrix} \sin 2\alpha & \cos 2\alpha \\ \cos 2\alpha & -\sin 2\alpha \end{bmatrix}. \qquad (43)$$

The calculation of a scalar quantity is implied by the Einstein summation notation, $\dot{\varepsilon}_{ij}\dot{\varepsilon}_{ij}$, which means that all the elements of the tensor are squared and summed (Ranalli, 1995, equation 4.20). Thus, after much algebra, the invariants reduce to (as they should be independent of orientation),

$$\dot{\gamma}_b^{II} = \dot{\varepsilon}_{ij}^b\dot{\varepsilon}_{ij}^b = \frac{1}{2}(b_{13})^2 \qquad (44)$$

and

$$\dot{\gamma}_n^{II} = \dot{\varepsilon}_{ij}^n\dot{\varepsilon}_{ij}^n = \frac{1}{2}(n_{13})^2. \qquad (45)$$

APPENDIX B: THE RELATIONSHIP BETWEEN α AND β

The following section describes the derivation of the relationship between α and β that is essential for solving the strain rates and thus the dissipation calculation. All constraints on the relationships between a_b, p_b, and the velocities and strain rates are derived from the vector diagram drawn in Fig. 3. We seek a relationship between α and β in terms of the parameters a_b and p_b. Using the trigonometric relations drawn in Fig. 3b,

$$\mathbf{v}_t = a_b\mathbf{v}_b + (1 - a_b)\mathbf{v}_n \qquad (46)$$

where

$$\mathbf{v}_t = \mathbf{Th}_t = \begin{bmatrix} 0 & t_{13} \\ 0 & 0 \end{bmatrix}\begin{bmatrix} 0 \\ h_t \end{bmatrix}, \qquad (47)$$

$$\begin{aligned} \mathbf{v}_b &= \mathbf{B}^R\mathbf{h}_b = \begin{bmatrix} b_{13}\sin(\alpha)\cos(\alpha) & b_{13}\cos(\alpha)^2 \\ -b_{13}\sin(\alpha)^2 & -b_{13}\sin(\alpha)\cos(\alpha) \end{bmatrix} \\ &\quad \times \begin{bmatrix} h_b\sin(\alpha) \\ h_b\cos(\alpha) \end{bmatrix} \end{aligned} \qquad (48)$$

and

$$\begin{aligned} \mathbf{v}_n &= \mathbf{N}^R\mathbf{h}_n = \begin{bmatrix} n_{13}\sin(\beta)\cos(\beta) & n_{13}\cos(\beta)^2 \\ -n_{13}\sin(\beta)^2 & -n_{13}\sin(\beta)\cos(\beta) \end{bmatrix} \\ &\quad \times \begin{bmatrix} h_n\sin(\alpha) \\ h_n\cos(\alpha) \end{bmatrix}. \end{aligned} \qquad (49)$$

Solving equation (3) yields two equations,

$$\begin{bmatrix} h_t t_{13} = a_b h_b b_{13}\cos(\alpha) + (1 - a_b)h_n n_{13}\cos(\beta)\cos(\alpha - \beta) \\ 0 = -a_b h_b b_{13}\sin(\alpha) - (1 - a_b)h_n n_{13}\sin(\beta)\cos(\alpha - \beta) \end{bmatrix}. \qquad (50)$$

We solve the bottom equation for n_{13} and substitute it in to the top one, and then substitute in the unit cell definitions

$$\frac{h_b}{h_t} = \frac{a_b}{\cos(\alpha)} \quad \text{and} \quad \frac{h_n}{h_t} = \frac{1-a_b}{\cos(\alpha)} \quad \text{and} \quad \frac{h_n}{h_b} = \frac{1-a_b}{a_b}$$

illustrated in Fig. 3 Finally, pulling β onto the left side gives

$$\tan(\beta) = \frac{-(a_b)^2 b_{13}\tan(\alpha)}{t_{13} - (a_b)^2 b_{13}}. \qquad (51)$$

Then, substituting in our definition of p_b, so that $b_{13} = p_b t_{13} \cos(2\alpha)$, we get the workable version

$$\tan(\beta) = \frac{(a_b)^2 p_b \cos(2\alpha)\tan(\alpha)}{(a_b)^2 p_b \cos(2\alpha) - 1} \quad (52)$$

which is plotted in Fig. 4. Again, this relationship does not affect the strain rate because we use the invariant to calculate the dissipation and viscosity.

APPENDIX C: THE RELATIONSHIP BETWEEN SHEAR STRESS AND MELT PRESSURE

The shear stress in the bands and lenses can be calculated from the relative strain rates and viscosities in the band and lenses. The values of these stresses provide perhaps a more physically intuitive view of the behavior of these equations than the dissipation does, and provide an avenue into further questions and problems of the dynamics of melt segregation. The solid pressure influences the fluid pressure and melt flows directly in response to gradients in the fluid pressure. Here, we outline a few simple relationships between the shear stress and the local melt and solid pressures. The aim is to motivate the questions of what pressure gradients may exist in the deforming systems that allow the melt to organize and continually readjust to maintain a constant average angle and a steady state.

As illustrated with a Mohr circle in Fig. A1, we define the various stress and pressure terms that we discuss below. Within the band and non-band regions, we define solid and fluid pressures, $\overline{P}_s^b$, P_f^b, $\overline{P}_s^n$ and P_f^n, respectively, where the overline indicates that the pressure is the mean stress, or

$$\overline{P} = \frac{\sigma_{11} + \sigma_{22} + \sigma_{33}}{3}. \quad (53)$$

If σ_{33} is equal to the confining pressure, P_c, and $\sigma_{22} \approx \sigma_{33}$, then

$$\overline{P} = \frac{(\sigma_{11} - \sigma_{33}) + 3\sigma_{33}}{3} = \frac{2}{3}\tau + P_c \quad (54)$$

where τ is the shear stress. Since P_c is constant in the sample, $\Delta \overline{P}_s^{b-n} = \frac{2}{3}(\Delta \tau_s^{b-n})$, where the shear stress difference is what we calculate in this analysis. We use the invariant of the deviatoric strain rate tensor as an approximation of the shear strain rate, such that $\tau \approx \eta(\frac{1}{2}\sqrt{\dot{\varepsilon}_{ij}\dot{\varepsilon}_{ij}})$ and $\Delta \tau_s^{b-n} = \tau_b - \tau_n = \eta_b \dot{\gamma}_b^{II} - \eta_n \dot{\gamma}_n^{II}$.

So the remaining question is how this shear stress or mean stress relates to the local fluid pressure? The fluid pressure is not defined as a mean stress because the shear stress in the fluid will be negligible (Fowler, 1990). Ultimately, when we calculate $\Delta \overline{P}_s^{b-n}$, we must relate it to ΔP_f^{b-n} in order to understand how deformation will affect melt flow. However, the relationship between
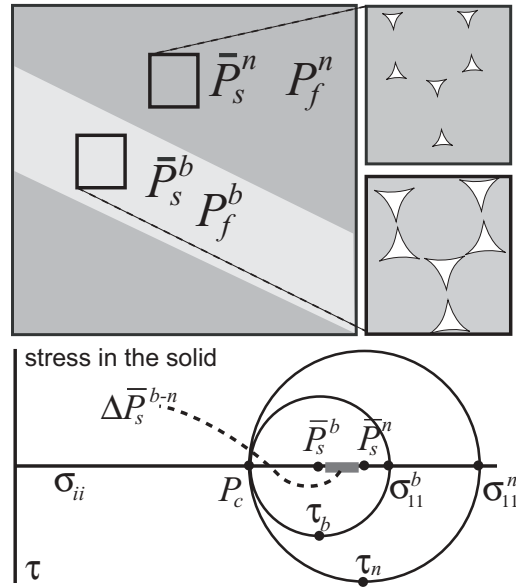

Fig. A1. The definition of the various pressures discussed in the analysis.

these two differentials is not clear. Within one element of a two-phase continuum, there exists a solid and a fluid pressure, for example, $\overline{P}_s^b$ and P_f^b. These two pressures are related by

$$\overline{P}_s - P_f = -\zeta\nabla\cdot\mathbf{v}_s \quad (55)$$

where $\nabla\cdot\mathbf{v}_s$ is the compaction rate and ζ is the bulk viscosity, which is probably strongly dependent on the melt fraction (McKenzie, 1984; Scott and Stevenson, 1986; Fowler, 1990). The form of this dependence is often assumed to be $\zeta \propto \phi^{-1}$. If $P_f > \overline{P}_s$, the melt pockets dilate, and if $\overline{P}_s > P_f$, they compact. Thus, if we knew the compaction rate and the bulk viscosity, we could determine a local melt pressure from this equation. However, the pressure gradient depends on the gradient of the shear strain rate and on the compaction/ decompaction rate (Spiegelman, 2003, equation 4). Because we are only looking at the differences in the contribution of shear deformation, in the present analysis, we cannot calculate this relationship, but only speculate in the Discussion. For the purpose of the analysis presented here, we make the simplest assumption that spatial gradients in fluid pressure will have the same sign as those in solid pressure in the same location.

Another factor affecting the fluid pressure is the surface tension, which relates the P_f to the curvature of melt-pocket walls (Stevenson, 1986; Cooper, 1990). When fluids tend to wet the grain boundaries (i.e. $2\gamma_{sf} > \gamma_{ss}$), surface tension tends to flatten perturbations in melt distribution and resist melt segregation. These effects are also not considered in this analysis.
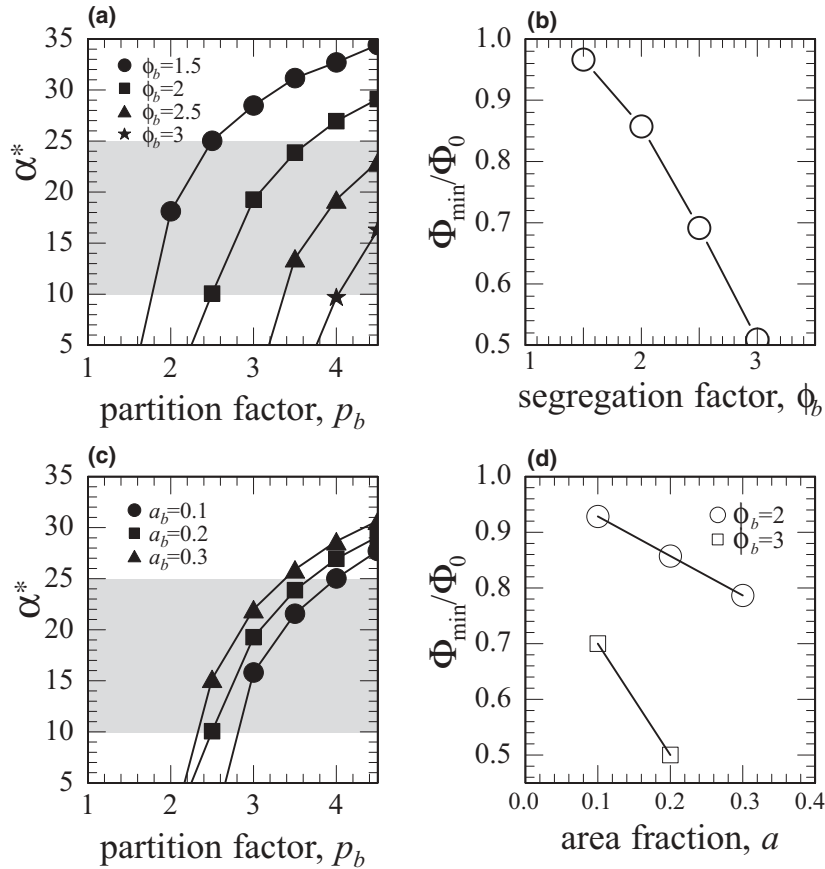
Fig. A2. Sensitivity tests. The minima in dissipation as a function of α vary with a_b, p_b and ϕ_b. All parameters are the same as in Fig. 7. (a) α^* as a function of p_b, with variable ϕ_b; (b) Φ_{min}/Φ_0 as a function of ϕ_b; (c) α^* as a function of p_b, with variable a_b; (d) Φ_{min}/Φ_0 as a function of a_b, for two values of ϕ_b.

APPENDIX D: SENSITIVITY TESTS

We systematically vary a_b, ϕ_b and p_b to explore the influence of a wide range of parameters on the values of the minima in dissipation and their dependence on band angle. The results, illustrated in Fig. A2, are plotted according to the following scheme. In the top row (Fig. A2a and b), the effects of varying ϕ_b are shown in two ways. In the bottom row (Fig. A2c and d), the effects of varying a_b are shown. In the left column (Fig. A2a and c), we plot the values of α associated with each minimum in dissipation, as a function of p_b for different values of ϕ_b (top) and for a (bottom). In the right column (Fig. A2b and d), we plot the normalized values of the dissipation where the minima occur, as functions of ϕ_b (top) and a_b (bottom), exploiting the observations above that the value of dissipation at the minima does not depend on α or p_b, but only on a_b and ϕ_b. The figures in the right column show the most basic and intuitive results: (1) the more that melt segregates into the bands (ϕ_b), the lower the energy dissipation; and (2) the larger the volume fraction of bands (a_b), the lower the energy dissipation. In other words, melt segregation and strain partitioning are

energetically favorable; the more the melt segregates, the lower the energy becomes and the weaker the rock becomes.

Varying ϕ_b. In Fig. A2a, we plot the influence of the partitioning factor p_b on the band angle at which Φ is minimized, α^*. The general trend of all slopes indicate that, as p_b increases, α^* increases, as seen in Fig. 7, for a fixed value of a_b and ϕ_b. As ϕ_b increases, a higher value of p_b is required to reach a minimum in dissipation at a given angle. In other words, at a given value of α, the weaker the bands are relative to the lenses, the more strain must concentrate in the bands to minimize the dissipation. As shown in Fig. A2b, as strain rate in the bands increases relative to the total, the absolute value of the dissipation drops quickly and almost linearly. The deviation from linearity comes from the fact that ϕ_b appears in the exponential term in the viscosity–ϕ relation, equation (19). For $a_b = 0.2$, a twofold increase in ϕ_b leads to a twofold decrease in dissipation.

Varying a_b. When a_b is varied (Fig. A2c and d), the curves of α^* vs p_b have a similar curvature as those when ϕ_b is varied. However, increasing a_b has the inverse

effect on α^* than increasing ϕ_b. At a constant value of p_b, increasing a_b causes an increase in α^*; or at a constant α^*, a decrease in a_b corresponds to an increase in p_b. To clarify the latter, the more the strain rate is concentrated in the bands, a smaller volume of (or fewer) bands is (are) needed to attain a minimum dissipation level at a certain angle. In Fig. A2d, Φ_{min} decreases linearly with increasing a_b, because a_b is simply a weighting factor on the dissipation values for the bands and lenses in equation (20) and for p_b in equation (34d and e). The total amount of dissipation reduction is much more sensitive to ϕ_b than to a_b. Finally, the effect of varying λ (not shown) on the relation of Φ to p_b is very similar to that caused by the variation of ϕ_b, because an increase in both essentially weakens the bands relative to the solid.